

## Research Paper

# Characterization of Magnetic Viral Complexes for Targeted Delivery in Oncology

Isabella Almstätter<sup>1\*</sup>, Olga Mykhaylyk<sup>2\*</sup>, Marcus Settles<sup>1</sup>, Jennifer Altomonte<sup>3</sup>, Michaela Aichler<sup>4</sup>, Axel Walch<sup>4</sup>, Ernst J. Rummeny<sup>1</sup>, Oliver Ebert<sup>3</sup>, Christian Plank<sup>2</sup> and Rickmer Braren<sup>1</sup>✉

1. Department of Diagnostic and Interventional Radiology, Klinikum rechts der Isar der Technischen Universität München, Munich, Germany;
2. Department of Experimental Oncology and Therapy Research, Klinikum rechts der Isar der Technischen Universität München, Munich, Germany;
3. II. Med. Clinic, Gastroenterology, Klinikum rechts der Isar der Technischen Universität München, Munich, Germany;
4. Research Unit Analytical Pathology, Institute of Pathology, Helmholtz Zentrum München, Neuherberg, Germany.

\* contributed equally.

✉ Corresponding author: email: rbraren@tum.de.

© 2015 Ivyspring International Publisher. Reproduction is permitted for personal, noncommercial use, provided that the article is in whole, unmodified, and properly cited. See <http://ivyspring.com/terms> for terms and conditions.

Received: 2014.08.29; Accepted: 2015.01.07; Published: 2015.03.18

## Abstract

Oncolytic viruses are promising new agents in cancer therapy. Success of tumor lysis is often hampered by low intra-tumoral titers due to a strong anti-viral host immune response and insufficient tumor targeting. Previous work on the co-assembly of oncolytic virus particles (VPs) with magnetic nanoparticles (MNPs) was shown to provide shielding from inactivating immune response and improve targeting by external field gradients. In addition, MNPs are detected by magnet resonance imaging (MRI) enabling non-invasive therapy monitoring.

In this study two selected core-shell type iron oxide MNPs were assembled with adenovirus (Ad) or vesicular stomatitis virus (VSV). The selected MNPs were characterized by high  $r_2$  and  $r_2^*$  relaxivities and thus could be quantified non-invasively by 1.5 and 3.0 tesla MRI with a detection limit below 0.001 mM iron in tissue-mimicking phantoms. Assembly and cell internalization of MNP-VP complexes resulted in 81 – 97 % reduction of  $r_2$  and 35 – 82 % increase of  $r_2^*$  compared to free MNPs. The relaxivity changes could be attributed to the clusterization of particles and complexes shown by transmission electron microscopy (TEM). In a proof-of-principle study the non-invasive detection of MNP-VPs by MRI was shown *in vivo* in an orthotopic rat hepatocellular carcinoma model.

In conclusion, MNP assembly and compartmentalization have a major impact on relaxivities, therefore calibration measurements are required for the correct quantification in biodistribution studies. Furthermore, our study provides first evidence of the *in vivo* applicability of selected MNP-VPs in cancer therapy.

Key words: magnetic viral complexes, nanoassembly, magnetic nanoparticles (MNPs), MRI relaxivity, MRI phantoms, oncolytic virus.

## Introduction

Magnetic nanoparticles (MNPs) are multi-functional tools that can be detected non-invasively at low concentrations by MRI. They have been widely employed in oncology, e.g. as contrast agents in tumor detection, as carriers in drug delivery [1-4] and magnetic drug targeting [5-8], as well as therapeutically in hyperthermia [9-11]. The diagnostic applica-

tions are based on magnetic properties [12, 13], chemical stability and biocompatibility [14] of MNPs that allow for non-invasive and real-time monitoring of systemically injected particles via magnet resonance tomography (MRI). MRI without contrast agents provides high spatial resolution and excellent soft tissue contrast [15]. To even further enhance its

sensitivity, iron oxide based contrast agents can be applied, exploiting their effect on tissue relaxation rates [16, 17].

Viral [18-20] and non-viral gene therapies [21] are rapidly developing modalities of cancer treatment. Several oncolytic viruses such as adenovirus (Ad) and vesicular stomatitis virus (VSV) are under investigation for direct therapeutic application. Oncolytic viruses specifically replicate in cancer cells [18-20] and are suitable either as single agents or in combination with chemotherapy and radiation therapy [22]. Ad, a double-strand DNA virus, has been tested for the treatment of several cancer types [20], [23]. In addition, Ad belongs to the category of the most powerful gene delivery systems [24]. VSV is a negative-stranded RNA virus, which specifically replicates in interferon deficient tumor cells. VSV has been successfully used preclinically for the treatment of various cancers, including multifocal hepatocellular carcinoma lesions (HCC) in rat models [25, 26].

Suitable core-shell type MNPs are known to form stable complexes with different virus particles by self-assembly [27-32]. This complex formation can enhance viral transduction efficiency and transgene expression of viral complexes via non-permissive cell infection [24, 27, 29, 30, 32-36] with enhanced internalization of viral and non-viral vector complexes due to an externally applied gradient magnetic field, a procedure referred to as magnetofection [37]. It enables site specific targeting of magnetically labeled virus particles with an external magnetic field. This way, limited infectivity can be overcome [29]. In addition, complex formation with MNPs minimizes the interaction with blood components and cells due to the shielding effect of the nanoparticles [24]. The shielding effect of the MNPs used in this study against virus neutralizing antibodies and the stability of the self-assembled complexes in serum-containing medium was proven in previous work [12, 29, 31].

In this study, we investigated the MRI contrast properties of selected core-shell MNPs and self-assembled MNP-VP complexes, both in suspension, and after internalization into different cell lines. Transmission electron microscopy (TEM) was used for visualization of MNPs, assembled MNP-VP complexes and intracellular compartmentalization. Samples were further characterized for their physical properties such as hydrodynamic diameter, electrokinetic (or zeta) potential and magnetophoretic mobility (magnetic responsiveness) and the ability to transfect cells in the presence of moderate and high serum concentrations and the resulting oncolytic effect *in vitro* in applied magnetic fields. We further provide a first outlook of the potential *in vivo* application of these new MNP-VP complexes.

## Experimental

### Synthesis and Physico-Chemical Characterization of Core-Shell Type Magnetic Nanoparticles

Core-shell type iron oxide MNPs were synthesized by precipitation of the Fe(II)/Fe(III) hydroxide from aqueous solution in an oxygen-free atmosphere, followed by transformation into magnetic iron oxide with spontaneous adsorption of the fluorinated surfactant Zonyl-FSA (lithium 3-[2-(perfluoroalkyl)ethylthio]propionate) (FSA) combined with 25-kDa branched polyethylenimine (PEI<sub>Br-25</sub> kDa) for PEI-Mag2 nanoparticles (further referred to as PEI-Mag particles) or condensation of tetraethyl orthosilicate (TEOS) and 3-(trihydroxysilyl)propylmethylphosphonate (THPMP) resulting in silicon oxide layer with surface phosphonate groups (Si-O<sub>x</sub>/Phosphonate) for SO-Mag5 nanoparticles as previously described [37, 38]. The resulting coated magnetic nanoparticle suspensions were dialyzed against ddH<sub>2</sub>O to remove unbound coating components and then sterilized using <sup>60</sup>Co gamma-irradiation with a dosage of 25 kGy [39]. For assembling with negatively charged virus particles, the SO-Mag5 nanoparticles were decorated with PEI at a PEI-to-iron (w/w) ratio of 11.5 % yielding SO-Mag6-11.5 nanoparticles, further referred to as SO-Mag particles. The particle stock concentrations in terms of dry weight and iron content were determined as described previously [37]. The average crystallite size of the core was calculated from the X-ray diffraction data using the Scherrer formula [40]. Mean hydrodynamic diameter  $D_h$  and electrokinetic zeta potential  $\zeta$  of the MNPs suspended in ddH<sub>2</sub>O were measured by photon correlation spectroscopy using a Malvern 3000 HS Zetasizer (Malvern Instruments Ltd., UK). The saturation magnetization per unit of iron weight  $M_s$  was measured at 298 K using a vibrating sample magnetometer (Oxford Instruments Ltd.).

### Cell Culture

The MDR human pancreatic carcinoma cells EPP85-181RDB, further referred to as RDB cells, were grown in Dulbecco's modified Eagle's medium (DMEM; Gibco®, Life Technologies, Darmstadt, Germany) supplemented with 10 % heat-inactivated fetal calf serum (FCS; Gibco®, Life Technologies, Darmstadt, Germany) and 1 % 2 mM L-glutamine (Gibco®, Life Technologies, Darmstadt, Germany). The rat Morris hepatocellular carcinoma cells (McA-RH7777), further referred to as McA cells, and the baby hamster kidney cells BHK-21 cells were purchased from the American Type Culture Collection (LGC Standards GmbH, Wesel, Germany), and were cultured in

DMEM (ATTC, Manassas, MA, USA) supplemented with 10 % heat-inactivated FCS, 100 U mL<sup>-1</sup> penicillin, and 100 µg mL<sup>-1</sup> streptomycin (all PAA Laboratories GmbH, Pasching, Austria). All cell lines were cultured at 37 °C in a humidified atmosphere containing 5 % CO<sub>2</sub>.

### Adenovirus and Vesicular Stomatitis Virus

The E1A mutant adenovirus dl520, further referred to as Ad, was kindly provided by Dr. Per Sonne Holm [41]. The Ad was expanded in 293 cells and purified by double cesium chloride gradient centrifugation, resulting in a virus stock containing 4.3 × 10<sup>12</sup> VP/mL and 2.6 × 10<sup>11</sup> TU/mL. To determine the physical virus particle titer, an aliquot of the virus stock was diluted 1 to 20 in Dulbecco's phosphate buffered saline (PBS; Gibco®, Life Technologies, Darmstadt, Germany) that contained 0.1 % sodium dodecyl sulphate, mixed thoroughly for 2 minutes and centrifuged at 8,000 g for 5 minutes. The optical density at 260 nm was measured, and the physical virus titer was calculated, taking into account that an OD of 1 corresponds to 1.1 × 10<sup>12</sup> VP/mL [42]. Aliquots of the stock were stored at -80 °C.

The rVSV-GFP, further referred to as VSV, was expanded in BHK-21 cells and the supernatant was purified by sucrose gradient centrifugation as previously described [25, 26] resulting in a virus stock containing 6.6 × 10<sup>9</sup> pfu/mL as was determined by plaque assay on BHK-21 cells. Aliquots of the stock were stored at -80 °C.

### Preparation of Magnetic Viral Complexes

Ad complexes with MNPs were prepared as described in detail previously [35]. Briefly, 10<sup>11</sup> VP of the Ad diluted in 800 µL PBS were added to 200 µL of PEI-Mag2 or SO-Mag6-11.5 MNPs in ddH<sub>2</sub>O containing 500 µg of Fe and mixed, resulting in an iron-to-physical virus particle ratio of 5 fg Fe/VP. The resulting complexes will be further referred to as PEI-Mag-Ad and SO-Mag-Ad complexes.

To prepare magnetic VSV complexes, equal volumes of ddH<sub>2</sub>O containing MNPs of 226.8 µg iron and PBS containing 4.5 × 10<sup>8</sup> pfu or 2.3 × 10<sup>8</sup> pfu VSV were mixed in a final volume of 1,380 µL. The resulting ratios of MNP-to-virus were of 500 and 1,000 fg Fe/pfu, respectively, for PEI-Mag2 and SO-Mag6-11.5 particles, respectively. The resulting complexes will be further referred to as PEI-Mag-VSV and SO-Mag-VSV complexes.

After an incubation period of 20 minutes at RT to allow complex assembly, the volume was adjusted with PBS and the freshly prepared complexes were used for characterization of the magnetic vectors, cell infection and phantom preparation.

### Magnetic Cell Labeling and Infection with Magnetic Viral Complexes

The cells were grown in 75 cm<sup>2</sup> cell culture flasks (Techno Plastic Products, Trasadingen, Switzerland) and loaded with MNPs or infected with magnetic viral complexes when they reached 70 to 80 % confluency (4 - 6 × 10<sup>6</sup> cells per flask). 25 and 10 pg iron per cell either in the form of free MNPs or their viral complexes with Ad or VSV were applied in cell culture medium to the RDB and McA cells, respectively. The applied complex doses corresponded to the MOI of 120 for the adenoviral complexes and MOIs of 20 (PEI-Mag-VSV) and 10 (SO-Mag-VSV) for infection with the VSV complexes. A magnetic field was then applied for the magnetofection [37] by positioning the flasks on a magnetic plate (OZ Biosciences, Marseille, France; field strength and gradient at the cell layer location of 70–250 mT and of 50–130 T/m, respectively) for 30 minutes in the case of the RDB cells [31] and 1 hour for the McA cells at 37 °C in the incubator. Afterwards, the RDB cells were incubated for another 3 hours in the incubator without magnetic field. The labeled cells were washed with PBS three times to remove any loosely-bound particles or complexes. Next, the cells were trypsinized using a 0.25 % trypsin/0.02 % EDTA solution (Gibco®, Life Technologies, Darmstadt, Germany). After washing with PBS, the cells were fixed with BD Cytifix™ (BD Biosciences, Heidelberg, Germany), washed three times with PBS and resuspended in PBS for use in cell characterization or phantoms preparation.

### Analysis of the Exogenic Non-Heme Iron Content of the Magnetically Labeled or Magnetofected Cells

The magnetically (virus-)labeled cells were analyzed by determination of the exogenic non-heme iron content as described elsewhere using the modification of the method of Torrance and Bothwell [37, 43]. Briefly, approximately 4 × 10<sup>5</sup> trypsinized cells were washed with PBS and spun down by centrifugation. The supernatant was discarded and the cell pellet was resuspended in 500 µL of an acid mixture containing 3 M HCl and 0.6 M trichloroacetic acid. After an overnight incubation at 65 °C, the samples were centrifuged and 50 µL of the clear supernatant were analyzed for the iron content by a colorimetric method with 1,10-phenanthroline. Therefore, the supernatant was mixed with 50 µL sterile water, 20 µL 10 % hydroxylamine-hydrochloride solution, 100 µL ammonium acetate buffer (25 g ammonium acetate and 70 ml glacial acetic acid with a total volume adjusted to 100 ml with ddH<sub>2</sub>O), and 50 µL 0.1 % 1,10-phenanthroline solution (all Fluka, Sigma-Aldrich, Steinheim, Germany and Roth, Karls-

ruhe, Germany). The mixture was incubated for 20 minutes, followed by measurement of optical density at 510 nm, which is the absorption maximum of the iron(II)-1,10-phenanthroline complex, in a Beckman DU 640 spectrophotometer (Beckman Coulter Inc., Krefeld, Germany). The iron content was calculated using a calibration curve measured for the freshly prepared dilution series of the iron stock solution (392,8 mg ammonium iron(II) sulfate hexahydrate, 2 mL concentrated H<sub>2</sub>SO<sub>4</sub> and 10 mL distilled water, titrated with 0.05 N KMnO<sub>4</sub> until a faint pink color persisted, followed by volume adjustment to 100 mL).

### Sample Preparation and Transmission Electron Microscopy (TEM)

For TEM analysis, about 10<sup>5</sup> labeled or infected cells were washed with PBS after trypsinization. Free MNP suspensions, free MNP-VP complexes, both containing about the same amount of iron as that applied to cells, and the cells were pelleted for 5 minutes at 1,600 rpm in beam tubes and the (cell) pellets were fixed with 2.5 % glutaraldehyde in 0.1 M sodium cacodylate buffer pH 7.4 TEM fixation buffer (Electron Microscopy Sciences, Hatfield, United States) at 4 °C. The samples were then post-fixed in 2 % aqueous osmium tetroxide [44], dehydrated in gradual ethanol (30 – 100 %) and propylene oxide, embedded in Epon (Merck, Darmstadt, Germany) and dried for 24 hours at 60 °C. Semithin sections were cut and stained with toluidine blue. Ultrathin sections of 50 nm were collected onto 200 mesh copper grids, stained with uranyl acetate and lead citrate before examination by transmission electron microscopy (Zeiss Libra 120 Plus, Carl Zeiss NTS GmbH, Oberkochen, Germany). Pictures were acquired using a Slow Scan CCD-camera and iTEM software (Olympus Soft Imaging Solutions, Münster, Germany).

### Characterization of the Oncolytic Potential of Magnetic Viral Complexes *In Vitro*

The RDB cells and McA cells were seeded in 96-well cell culture plates at 10<sup>4</sup> cells per well and incubated at 37 °C 24 hours prior to infection. The cell culture medium in each well was replaced with 150 µL of fresh culture medium containing 10 % FCS (or 66.7 % FCS), and 50 µL of virus or the magnetic viral complexes in serum free medium were added. The resulting medium was referred to as the infection medium with a final FCS concentration of 7.5 % (or 50 %). To define the concentration required for 50 % cell growth inhibition (IC<sub>50</sub>) for free virus or viral complexes, 2-to-1 serial dilutions of naked adenovirus ranging from 2.5–320 pfu/cell and from 0.625–80 pfu/cell for the MNP-Ad complexes, and MOIs of

0.005-10 for naked VSV and the MNP-VSV complexes were prepared, all in triplicates. If indicated, a magnetic field was applied by positioning the cell culture plates on a magnetic plate for 30 minutes. No medium change was performed and the RDB and McA cells were incubated for 6 days and 24 hours, respectively.

The survival of infected RDB cells was evaluated 6 days after infection using a luciferase assay as described elsewhere [37]. Briefly, the cells were washed with PBS and lysed with 100 µL of lysis buffer per well. After incubation for 15–20 minutes at RT, 50 µL of cell lysate in each well was transferred to the wells of a 96-well black flat-bottom plate. Then, 100 µL of D-luciferin buffer was added. The chemiluminescence intensity was measured in counts per min (CPM) using a Microplate Scintillation & Luminescence Counter (Packard Instrument Co., Inc./Canberra Industries, Meriden, CT, USA). The uninfected cells were used as a reference control and taken to represent 100 % viable cells. The empty wells with a mixture of 50 µL of lysis buffer and 100 µL of D-luciferin buffer were used as blanks. The cell survival was computed according to the following equation:

$$\text{Cell survival (\%)} = \frac{(CPM_{\text{infected cells}} - CPM_{\text{blank}})}{(CPM_{\text{uninfected cells}} - CPM_{\text{blank}})} \times 100$$

The viability of the McA cells was assessed 24 hours after infection of the cells by the MTT assay as described elsewhere [37]. Briefly, infected cells were washed with PBS and 100 µL of MTT solution were added per well. After 2 hours incubation at 37 °C, viable cells formed formazan crystals in their mitochondria and those were lysed with 100 µL solubilization solution, overnight incubation at RT in the dark. The solvated crystals, representing the respiration activity of the cells, were quantified with a Wallac 1420 VICTOR<sup>2</sup> microplate reader (PerkinElmer, Waltham, MA, USA) at a wavelength of 590 nm. To evaluate the effect of free MNPs on the viability, the cells were treated with MNPs and analyzed under the same conditions.

The cell survival data were plotted against logarithms of the applied virus dose (pfu/cell) and were fitted using the “DoseResponse” function of OriginPro 9G software (OriginLab Corporation, Northampton, MA, USA) to determine the doses of virus resulting in 50 % cell growth inhibition (IC<sub>50</sub> values).

### Magnetophoretic Mobility Measurements of Viral Complexes and Complex Labeled Cells

To characterize the magnetic responsiveness of the magnetically labeled cells and the MNP-VP complexes, the time course of the decreasing turbidity of the suspensions when subjected to inhomogeneous

magnetic fields was measured, as previously described [45, 46]. Briefly, a gradient field was generated by positioning two mutually attracting packs of four quadrangular neodymium-iron-boron permanent magnets symmetrically on each side of a cuvette holder, parallel to a beam of light, for optical density measurements. The magnetic field between the magnets was measured with a Hall detector using a grid of step size 1 mm, and the average magnetic field and the resulting field gradient were calculated to be 0.213 T and  $4 \pm 2$  T/m in the direction of the complex movement. The complex and cell suspensions were diluted to 500  $\mu$ L aliquots to achieve a starting optical density (OD) of OD = 0.3–1 at the analytical wavelength of 610 nm for the labeled cells and 360 nm for the magnetic viral complexes. Optical cuvettes filled with these diluted suspensions were placed in a Beckman DU 640 spectrophotometer and the change in the optical density or turbidity was immediately recorded over 30 minutes.

### Preparation of Calibration Phantoms for MR Imaging

Calibration phantoms for MR imaging with agarose gel containing homogeneously dispersed free MNPs, free MNP-VP complexes, cells labeled with MNPs and cells infected with MNP-VP complexes, respectively, were prepared in 24-well plates (Techno Plastic Products, Trasadingen, Switzerland) as described elsewhere [12, 13]. Briefly, according to Christoffersson *et al.* tissue-mimicking phantom material can be prepared by using different concentrations of nickel and agarose [47]. Increasing nickel (II) ion concentration shifts the  $T_1$  values to longer relaxation times, while increasing agarose concentration results in  $T_2$  relaxation time shortening. The gel phantom mimicking relaxivity of murine liver tissue ( $T_1 = 550$  ms and  $T_2 = 48$  ms; data not shown) was prepared with 198 mM  $\text{Ni}(\text{NO}_3)_2$ , 2.45 % agarose (Biozym, Oldendorf, Germany) and 0.5 % sodium azide for preservative purposes.

Dilution series (samples were diluted 2-to-3) were prepared for all samples, in water for free MNPs, and in PBS for free MNP-VP complexes and magnetically labeled and infected cells. The maximal iron [in mM Fe/well] and cell [in cells/mL] concentrations present in well 1, as well as the respective cell labeling [in pg Fe/cell] and labeling efficiencies are summarized in table 1. To provide proof of the detectability of the MNP iron in surrounding liver tissue and to exclude air artifacts during the magnet resonance image acquisition, the 12 wells between the sample wells, and the cavities between the wells on both sides were filled with the described Ni-containing agarose gel. For the 11 sample wells and the reference well

(positions of the experimental wells are shown in the photograph of figure 7A), gel with 1.5-fold higher concentrations of the nickel salt, agarose and sodium azide was prepared and 3 mL of to 60 °C pre-warmed agarose gel were vortex-mixed with 1.5 mL sample in 15 mL falcon tubes to distribute the nanomaterial homogeneously, and transferred into the designated well avoiding air bubbles. Well R contained only water/PBS mixed with this agarose gel and served as a reference well for background normalization. To identify potential relaxivity changes caused by the cell background, phantom plates with untreated, fixed cells were prepared in the same manner. The phantom plates were allowed to cool down slowly to room temperature, and were sealed with parafilm to avoid evaporation of water during the storage at 4 °C.

### MR Imaging

The imaging experiments were performed on a clinical 1.5 T MRI system (1.5 T Achieva, Philips Medical System, Best, the Netherlands) and a clinical 3.0 T MRI system (3.0 T Ingenia, Philips Medical System, Best, the Netherlands) using the 8-channel SENSE head coil for signal reception. The rectangular agarose phantom plates were centrally positioned on the head cushion of the coil.  $T_2$  and  $T_2^*$  maps of the calibration phantoms were measured using the following sequences on the 1.5 T MRI system: for  $T_2$  a multi-spin echo sequence with  $T_R = 2,000$  ms,  $TE = n \times 4.9$  ms ( $n = 1 \dots 30$ ), flip angle = 90 °, FOV = 160 x 88, resolution = 1 x 1 x 3 mm<sup>3</sup>, 3 slices of 3 mm thickness with gap = 0 mm, scan time = 6:04 minutes and for  $T_2^*$  a multi-echo gradient echo sequence (FFE) with  $TR = 1000$  ms,  $TE = 2.1 + n \times 3.2$  ms ( $n = 0 \dots 15$ ), flip angle = 90 °, FOV = 160 x 92, resolution = 1 x 1 x 3 mm<sup>3</sup>, 3 slices of 3 mm thickness with gap = 0 mm, scan time = 4:40 minutes. On the 3.0 T system the sequences were the following: for  $T_2$  a multi spin echo sequence with  $T_R = 2,200$  ms,  $TE = n \times 6.0$  ms ( $n = 1 \dots 30$ ), flip angle = 90 °, FOV = 160 x 88, resolution = 1 x 1 x 2 mm<sup>3</sup>, 7 slices of 2 mm thickness with gap = 0 mm, NSA = 1, scan time = 5:47 minutes and for  $T_2^*$  a FFE with  $TR = 1500$  ms,  $TE = 2.2 + n \times 2.7$  ms ( $n = 0 \dots 15$ ), flip angle = 90 °, FOV = 160 x 92, resolution = 1 x 1 x 2 mm<sup>3</sup>, 7 slices of 2 mm thickness with gap = 0 mm, NSA = 2, scan time = 7:28 minutes.

$T_2$  maps were calculated from the multi-spin echo data using the standard MR scanner mono-exponential fitting routine. For the  $T_2^*$  maps, the complex data of the multi-gradient echo sequence were analyzed using the RelaxMapsTool (Philips PRIDE data evaluation software package, Philips Medical System, Best, the Netherlands). This tool calculates  $B_0$  maps for all slices and – as a first order deviation from a mono-exponential signal decay –

takes into account the sinus-shaped oscillation of the multi-echo signal induced by the through plane  $B_0$  gradient [48].

For analysis, circular regions of interest (ROIs) were manually drawn for each well and the mean ( $\pm$  standard deviation (SD))  $R_2$  values were calculated from the  $T_2$  values. The  $R_2^*$  values of the manually drawn ROIs were extracted from the RelaxMapsTool. The mean  $R_2$  and  $R_2^*$  values  $\pm$  SD were calculated over the three slices scanned in all phantoms and the mean values were plotted against the iron concentration to determine the corresponding transverse relaxivities ( $r_2$  and  $r_2^*$ , [ $\text{mM}^{-1} \text{Fe s}^{-1}$ ]) by linear regression.

Mean basal relaxation rates at  $0 \mu\text{g Fe/mL}$  were:  $R_{2\text{max}} = 3.91 \pm 5.77 \text{ s}^{-1}$  and  $R_{2\text{max}}^* = 2.51 \pm 3.03 \text{ s}^{-1}$  for untreated McA cells (maximal cell concentration of  $1.91 \times 10^6 \text{ cells/mL}$ ) and  $R_{2\text{max}} = 1.74 \pm 0.37 \text{ s}^{-1}$  and  $R_{2\text{max}}^* = 5.07 \pm 0.86 \text{ s}^{-1}$  for untreated RDB cells (maximal cell concentration of  $3.36 \times 10^6 \text{ cells/mL}$ ).

### In Vivo Targeting of SO-Mag-VSV Complexes

All procedures involving animals were approved and performed according to the guidelines of the Institutional Animal Care and Use Committee, and the local government. Six-week-old male Buffalo rats, weighing 200 g, were purchased from Harlan Winkelmann (Borchen, Germany) and housed in a specific pathogen-free environment under standard conditions.  $10^6$  McA cells suspended in  $20 \mu\text{L}$  of DMEM were implanted orthotopically into the liver. After 10 days, the size of HCC nodules was determined by  $T_2$ -weighted MRI scans to be 0.5–1 cm in diameter.  $100 \mu\text{L}$  of complexes consisting of  $10^7$  pfu of VSV-GFP and  $10 \mu\text{g}$  iron of SO-Mag6-11.5 (ratio of 1,000 fg Fe/pfu of virus) or  $10^7$  pfu of naked VSV-GFP were injected intra-tumorally into orthotopic HCC nodules in the presence of a magnet placed on the surface of the tumor nodule opposite to the injection site. Magnets were left in place for 30 minutes following injection. To evaluate intra-tumoral virus titer and non-heme iron, animals were sacrificed 30 minutes post infection with SO-Mag-VSV complexes or naked VSV and whole tumors were sampled. To quantify delivered VSV,  $\text{TCID}_{50}$  analysis was performed on BHK-21 cells with whole tumor extracts. In addition, tumors were processed for quantification of non-heme iron content. An additional group of animals were imaged by MRI at 24 hours post infection to visualize accumulated of SO-Mag-VSV complexes. Subsequently, tumor and liver sections were fixed overnight in 4 % paraformaldehyde for histological and immunohistochemical analysis.

## Results

### Preparation and Characterization of Magnetic Nanoparticles (MNPs) and Self-Assembled Magnetic Viral Complexes (MNP-VPs)

Selected MNPs exhibited similar core diameters (PEI-Mag = 9.0 nm and SO-Mag = 6.7 nm). The saturation magnetization of the core material at RT was 62 and  $94 \text{ Am}^2/\text{kg}$  (Fe), resulting in an average magnetic moment of the insulated particles of  $5.8 \times 10^{-20}$  and  $8.7 \times 10^{-20} \text{ Am}^2$  for the PEI-Mag and the SO-Mag MNPs, respectively [37, 49]. Surface coating of PEI-Mag MNPs with a self-assembling layer comprising 32 mass% polyetheleneimine (PEI) and 68 mass% of the fluorinated surfactant Zonyl-FSA (figure 1A and C) resulted in a mean hydrodynamic diameter ( $D_h$ ) of  $28 \pm 2 \text{ nm}$ . In contrast, decoration of SO-Mag MNPs with PEI resulted in  $\text{SiO}_x$ /Phosphonate-PEI coating of 11.5 w/w% PEI-to-iron [38] (shown schematically in figure 1B) with a silica coating width of approximately 1 nm and a higher mean  $D_h$  of  $76 \pm 27 \text{ nm}$ , suggesting small aggregate formation. In addition, PEI coating led to a highly positive electrokinetic potential ( $\zeta$ ) for both MNPs ( $55.0 \pm 0.7 \text{ mV}$  for PEI-Mag and  $40.4 \pm 0.4 \text{ mV}$  for SO-Mag). The decreased potential of the SO-Mag particles compared to the PEI-Mag particles is due to the lower PEI content and the negatively charged surface phosphonate groups decorating the silica coating. On the other hand, mean  $D_h$  of selected viruses, Ad and VSV, were  $123 \pm 33 \text{ nm}$  and  $175 \pm 61 \text{ nm}$ , and both viruses exhibited a negative  $\zeta$  ( $-9.1 \pm 1.3 \text{ mV}$  and  $-11.8 \pm 0.7 \text{ mV}$ , respectively), enabling self-assembly of MNPs and VPs by electrostatic interactions. Complex formation with PEI-Mag resulted in a net positive charge of the magnetic viral complexes (PEI-Mag-Ad  $\zeta = 14.1 \pm 2.2 \text{ mV}$  and PEI-Mag-VSV  $\zeta = 15.1 \pm 0.8 \text{ mV}$ ). Co-assembly of SO-Mag with Ad also resulted in a net positive charge (SO-Mag-Ad  $\zeta = 13.6 \pm 0.4 \text{ mV}$ ), while a net negative charge was detected with VSV (SO-Mag-VSV  $\zeta = -7.1 \pm 0.8 \text{ mV}$ ).  $\zeta$  and  $D_h$  measurements of the different MNP-VP complex suspensions showed neither free MNPs nor naked VPs (data not shown). As expected, MNP-VP complexes were larger compared to naked VPs and larger for SO-Mag- compared to PEI-Mag-based complexes (PEI-Mag-Ad  $D_h = 271 \pm 178$  and PEI-Mag-VSV  $D_h = 514 \pm 99 \text{ nm}$ ; SO-Mag-Ad  $D_h = 609 \pm 127 \text{ nm}$  and SO-Mag-VSV  $D_h = 923 \pm 120 \text{ nm}$ ), the latter results suggesting aggregate formation of SO-Mag-VP complexes in PBS suspensions as well. Figure 2 shows a schematic of self-assembly of MNPs and VPs and the resulting magnetic viral complexes and table 2 summarizes their physico-chemical properties.

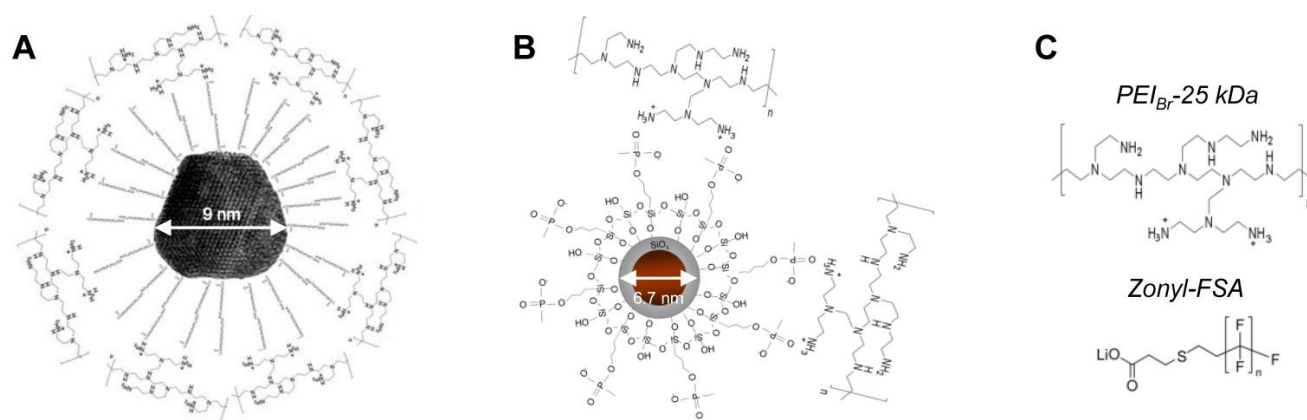


**Figure 1: Core-shell type MNP schematics and their coating components for assembling with virus particles.** **A** PEI-Mag2 particle coating comprises 32 mass% PEI<sub>B</sub>-25 kDa and 68 mass% Zonyl-FSA. **B** The silica-iron oxide MNPs SO-Mag6-11.5 are decorated with PEI<sub>B</sub>-25 kDa in a PEI-to-Fe w/w ratio of 11.5%. **C** Structural formulas of the 25 kD branched polyethyleimine (PEI<sub>B</sub>-25 kDa) and the fluorinated surfactant Zonyl FSA (n = 10, M<sub>w</sub> = 657.9 from XPS data), both used for nanoparticle coating.

**Table 1: Phantom characteristics** with MNPs, MNP-VPs, MNP labeled cells and MNP-VP infected cells. The maximal concentration was diluted in a 2-to-3 dilution series.

Sample	Maximal iron concentration	Maximal cell concentration	Cell labeling	Applied iron	Labeling efficiency
	[mM]	[10 <sup>6</sup> cells/mL]	[pg Fe/cell]	[pg Fe/cell]	[%]
PEI-Mag2	0.07	-	-		
SO-Mag6-11.5	0.32	-	-		
PEI-Mag2-VSV	0.11	-	-		
SO-Mag6-11.5-VSV	0.11	-	-		
PEI-Mag2-Ad	0.33	-	-		
SO-Mag6-11.5-Ad	0.33	-	-		
PEI-Mag2 in McA	0.14	1.74	4.5	10	45
SO-Mag6-11.5 in McA	0.2	2.05	5.4	10	54
PEI-Mag2-VSV in McA	0.22	3.88	3.2	10	32
SO-Mag6-11.5-VSV in McA	0.2	4.36	2.5	10	25
McA untreated	-	1.91	-	-	
PEI-Mag2 in RDB	0.79	2.55	17.3	25	69
SO-Mag6-11.5 in RDB	0.72	2.53	15.9	25	64
PEI-Mag2-Ad In RDB	0.11	0.90	6.7	25	27
SO-Mag6-11.5-Ad In RDB	0.14	1.03	7.4	25	30
RDB untreated	-	3.36	-	-	

**Table 2: Hydrodynamic diameter (D<sub>h</sub>) and electrokinetic potential (ζ) of free MNPs, VPs and MNP-VP complexes.**

Sample	Hydrodynamic diameter D <sub>h</sub> [nm]		Electrokinetic potential ζ [mV]	
	Peak position	Peak width	Mean	SD
<i>in water</i>				
PEI-Mag2	28	2	55.0	0.7
SO-Mag6-11.5	76	27	40.4	0.4
<i>in PBS</i>				
Ad	123	33	-9.1	1.3
VSV	175	61	-11.8	0.7
PEI-Mag2-Ad	271	178	14.1	2.2
SO-Mag6-11.5-Ad	609	127	13.6	0.4
PEI-Mag2-VSV	514	99	15.1	0.8
SO-Mag6-11.5-VSV	923	120	-7.1	0.8

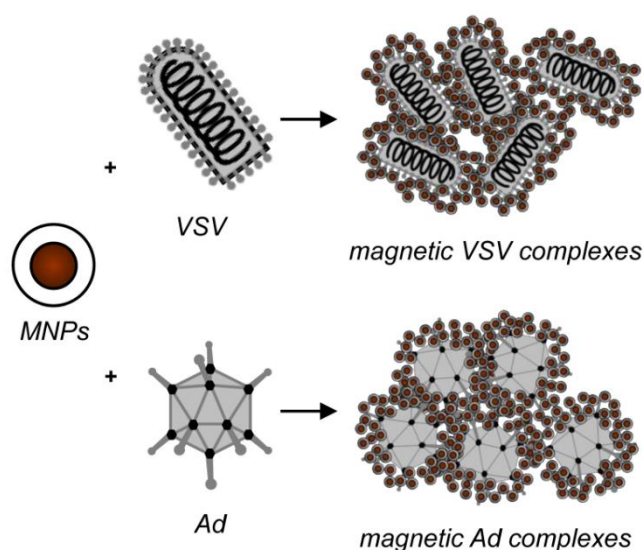


**Figure 2:** Schematics of the self-assembly of MNPs and virus particles into MNP-VP complexes.

### Highly Efficient Magnetic Cell-Labeling with MNPs or MNP-VP Complexes

To test cell-labeling efficiency of MNPs and MNP-VP complexes, two cell lines underwent magnetofection. Both, MNPs or MNP-VP complexes, resulted in high cellular iron loading (2.5 pg Fe/cell up to 17.3 pg Fe/cell upon application of 10 or 25 pg Fe/cell; table 1). No significant differences were detected between PEI-Mag and SO-Mag MNPs in iron loading. However, differences were evident between MNPs and magnetic viral complexes and between the different cell lines employed: MNP labeling resulted in higher iron loading compared to MNP-VPs (45 - 69 % to 25 - 32 % labeling efficiency, respectively) and RDB cells showed a higher uptake than McA cells for free MNPs (69/64 % to 45/54 % labeling efficiency) but not for MNP-VP-complexes (table 1). To avoid false positive results from background contamination, non-labeled cells were also analyzed for their iron content, and neither cell line revealed detectable levels of exogenous non-heme iron. Based on the obtained iron loading data, an efficient internalization of the magnetic nanomaterial was suggested.

### Transmission Electron Microscopy Analysis of Internalized MNPs and MNP-VP Complexes

To investigate the arrangement and aggregation of free and intracellular MNPs and MNP-VP complexes as well as their intracellular localization, transmission electron microscopy (TEM) was performed. Figure 3 shows TEM images of free MNPs and the different MNP-VP complexes for both types of VPs and MNPs. The suspended MNPs and MNP-VP complexes were mostly dispersed. Figure 4

compiles representative photomicrographs of the MNP and MNP-VP complex internalization in both cell lines. Free MNPs mainly clustered in the cytoplasm, in the RDB cells in endosomes while in McA cells the particles are more dispersed in the cytoplasm (figure 4, top row). In contrast to the free particles, MNP-VP complexes were localized exclusively in endosomes, independent of the cell type. Inside the endosomes, the magnetic and viral particles were arranged in a similar aggregate structure as the free MNPs in the cytoplasm.

### Characterization of the Oncolytic Potential of Magnetic Viral Complexes *In Vitro*

Figures 5A and B and table 3 displays the virus dose required for 50 % cell growth inhibition/oncolysis ( $IC_{50}$ ). The concentration-oncolytic effect curves registered for magnetic complexes of VSV and Ad with both MNPs were significantly shifted to low applied virus doses relative to the dose-effect curve of the virus alone. Even without magnetic field induction, the magnetic complexes were 1.2- to 6-fold more efficient than the naked virus in terms of the  $IC_{50}$  values of the applied dose (figure 5C and Supplementary Material: table S1). The  $IC_{50}$  values of the MNP-VP complexes under magnetic field-guided infection at 7.5 % FCS were 1.6- and 2.5-fold lower for VSV, and 11.8- and 27.4-fold lower for Ad, respectively, than those of the naked virus, emphasizing the higher oncolytic activity of the MNP-VP complexes (figure 5C and table 3). High serum concentration had a strong inhibitory effect on the oncolytic potency of the naked viruses and some effect on the complexes when no magnetic field was applied. However, for the magnetic complexes, magnetic field influence had about 10-fold and 2-fold enhancing effect on the oncolytic potency of the adenoviral and VSV complexes, respectively. This enhancement was true for low and high serum concentrations. The PEI-Mag-Ad complexes were hardly affected by serum in terms of the  $IC_{50}$ . High serum had only limited inhibitory effect on the  $IC_{50}$  of the SO-Mag-Ad and magnetic VSV complexes. Thus, *in vitro* results demonstrated enhancement of the oncolytic efficacy of the studied magnetic VSV and Ad complexes in McA and RDB cells at both, low and high serum concentrations.

### Magnetophoretic Mobility Measurements MNPs, MNP-VP Complexes and Labeled Cells

As expected, MNPs, MNP-VP complexes and loaded cells were responsive to an externally applied magnetic field as indicated by a decrease in the relative OD of their suspensions under the magnetic field (figure 6). The decrease in OD of the magnetic sam-

ples was due to the accelerated clearance imparted by the magnetic properties, whereas unlabeled cells simply sediment over time. From these turbidity clearance curves, the average magnetophoretic mobility of MNP-VP complexes and MNP- or MNP-VP-labeled cells, and the average number of MNPs associated with the complex or cell were calculated (table 4). Such complexes comprise  $2.2 \times 10^4$  PEI-Mag MNPs per virus particle for the complexes with VSV and  $2.6 \times 10^4$  MNPs per complex with Ad. The complexes with SO-Mag particles were larger and had more associated MNPs per complex ( $7.7 \times 10^4$  MNPs per VSV and  $2.2 \times 10^5$  MNPs per Ad). The mean hydrodynamic diameters of the MNP-VP complexes of about 500 nm, 270 nm, 900 nm and 600 nm (table 2), respectively, suggest that the complexes consisted of few physical virus particles surrounded with the

evaluated number of MNPs. In addition to the information about the complex sizes and compositions, it could be evaluated how many free and nanoassembled magnetic particles were taken up by the cells. There was an uptake of  $6.6 \times 10^5$  to  $7.0 \times 10^5$  MNPs per McA cell ( $16.3 \mu\text{m}$  in diameter) and  $8.4 \times 10^5$  to  $8.7 \times 10^5$  free magnetic particles by the RDB cells ( $16.5 \mu\text{m}$  in diameter) (table 4). The McA cells were infected with 15 and 36 MNP-VSV complexes and the RDB cells were infected with about 5 and 19 adenoviral SO-Mag- and PEI-Mag-complexes, respectively. The turbidity clearance time course under magnetic field application indicated an optimum of 30 minutes incubation time on the magnet (i.e. time needed for complete magnetic sedimentation) for the *in vitro* labeling and magnetotransduction experiments.

**Table 3: Virus dose required for 50 % cell growth inhibition/oncolysis (IC<sub>50</sub>)** 24 hours after infection of McA cells with MNP-VSV complexes and 6 days after Infection of RDB cells with MNP-Ad complexes for naked virus and its complexes with MNPs and the influence of magnetic field and FCS.

Sample	magnetic field		no magnetic field	
	7.5 % FCS	50 % FCS	7.5 % FCS	50 % FCS
<i>IC<sub>50</sub> in McA cells</i>				
VSV	0.106 ± 0.011	0.684 ± 0.167	0.155 ± 0.031	1.020 ± 0.139
PEI-Mag2-VSV	0.042 ± 0.003	0.087 ± 0.015	0.094 ± 0.013	0.169 ± 0.024
SO-Mag6-11.5-VSV	0.067 ± 0.0134	0.098 ± 0.021	0.085 ± 0.0107	0.180 ± 0.025
<i>IC<sub>50</sub> in RDB cells</i>				
Ad	48.7 ± 2.0	122.2 ± 31.9	44.3 ± 2.5	163.2 ± 3.8
PEI-Mag2-Ad	4.1 ± 0.3	4.4 ± 0.3	36.6 ± 3.4	43.2 ± 1.8
SO-Mag6-11.5-Ad	1.8 ± 0.1	2.8 ± 0.24	16.0 ± 0.8	36.5 ± 2.0

**Table 4: Physicochemical characteristics of MNP-VP complexes, MNP-labeled cells and MNP-VP infected cells.**

Sample	Time for magnetic sedimentation of 90% of complexes/cells	Magneto-phoretic mobility	Magnetic moment	Number of associated MNPs
	T <sub>0.1</sub> [s]	v <sub>z</sub> [ $\mu\text{m/s}$ ] <sup>a,b</sup>	M [ $\text{fAm}^2$ ] <sup>a</sup>	N = M/m <sub>eff</sub> <sup>c</sup>
PEI-Mag2-VSV	575	1.7	1.9	$2.2 \times 10^4$
PEI-Mag2-Ad	513	2.0	2.2	$2.6 \times 10^4$
SO-Mag6-11.5-VSV	441	2.3	4.4	$7.7 \times 10^4$
SO-Mag6-11.5-Ad	85	11.8	12.3	$2.2 \times 10^5$
PEI-Mag2 in McA	569	1.8	60.0	$7.0 \times 10^5$
SO-Mag6-11.5 in McA	911	1.1	37.5	$6.6 \times 10^5$
PEI-Mag2-VSV in McA	493	3.0	69.3	$8.0 \times 10^5$
SO-Mag6-11.5-VSV in McA	532	1.9	64.2	$1.1 \times 10^6$
PEI-Mag2 in RDB	480	2.1	72.0	$8.4 \times 10^5$
SO-Mag6-11.5 in RDB	706	1.4	49.0	$8.7 \times 10^5$
PEI-Mag2-Ad in RDB	822	1.2	42.1	$4.9 \times 10^5$
SO-Mag6-11.5-Ad in RDB	556	1.8	62.2	$1.1 \times 10^6$

<sup>a</sup> measured at an average magnetic field of  $B = 0.213 \pm 0.017$  T.

<sup>b</sup> measured at an average magnetic field gradient of  $\nabla B = 4 \pm 2$  T/m.

<sup>c</sup> m<sub>eff</sub> is an average effective magnetic moment of an insulated MNP

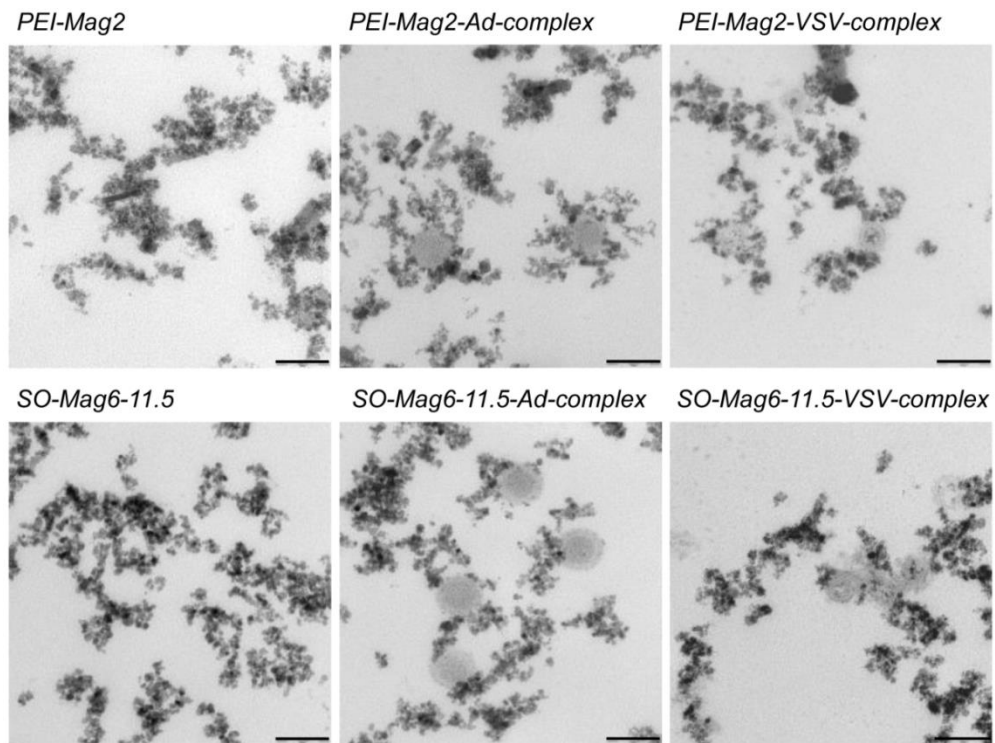


**Figure 3: Transmission electron microscopy.** TEM images of the suspended MNPs and the respective MNP-VP complexes for both types of MNPs and VPs. The scale bars are 100 nm.

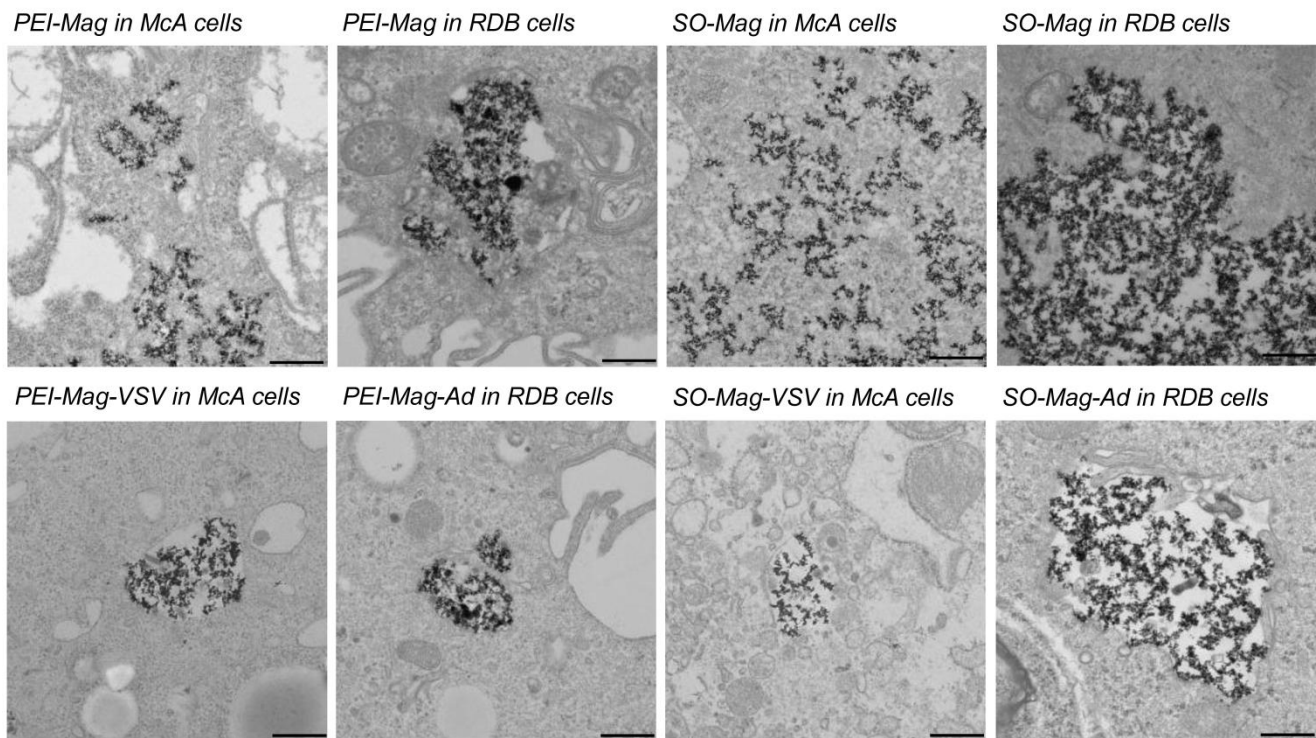


**Figure 4: Transmission electron microscopy.** TEM images of magnetically labeled and transduced cells for both cell lines and MNP-VP complexes. The scale bars are 500 nm.

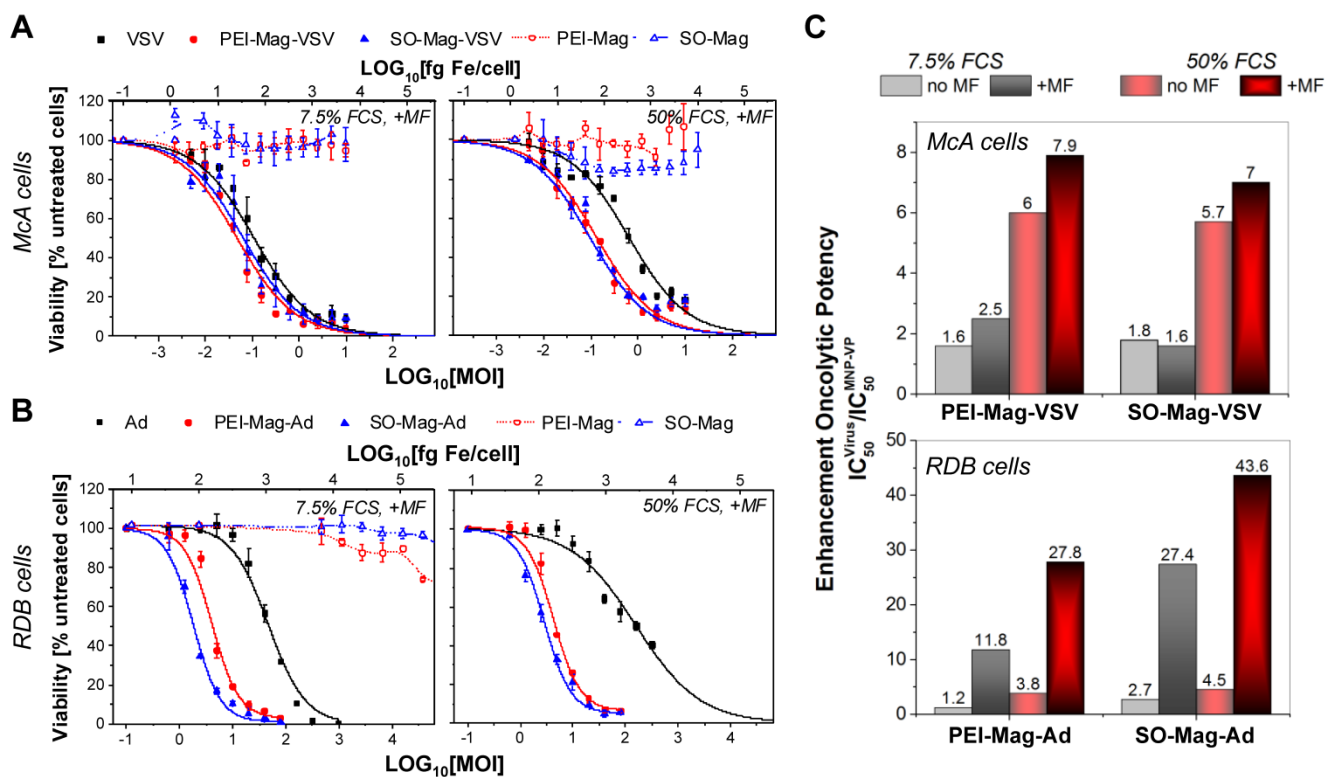


**Figure 5: Oncolytic activity of the magnetic viral complexes at moderate and high FCS concentrations.** **A** McA and **B** RDB cells were infected with naked virus or MNP-VP complexes at different virus doses under magnetic field application (+MF) for 30 minutes at FCS concentrations of 7.5 % (left panels) and 50 % (right panels). Oncolytic activity of the viruses and their magnetic complexes was assessed by measuring cell viability 24 hours after infection of McA cells using the MTT assay and 6 days after infection of the RDB cells expressing firefly luciferase using luciferase assay and expressed as a percentage using the untreated cells as a reference (mean ± SD; n = 3). Cell viabilities after treatment with equivalent doses of free MNPs are given as references. Naked virus is plotted in black, SO-Mag particles and their complexes in blue and PEI-Mag particles and their complexes in red. Panel **C** represents enhancement of oncolytic activity of the virus due to assembling with magnetic nanoparticles calculated as  $IC_{50}^{virus} / IC_{50}^{MNP-VP}$ , where  $IC_{50}^{virus}$  and  $IC_{50}^{MNP-VP}$  are virus doses per cell required for 50 % cell growth inhibition/oncolysis after infection with virus or its magnetic complexes deduced from the dose-response curves registered after infection under magnetic field (+MF, data shown in figures **A** and **B**) or without magnetic field (no MF, data not shown) application and different FCS concentrations (grey bars: 7.5 % FCS, red bars: 50 % FCS).

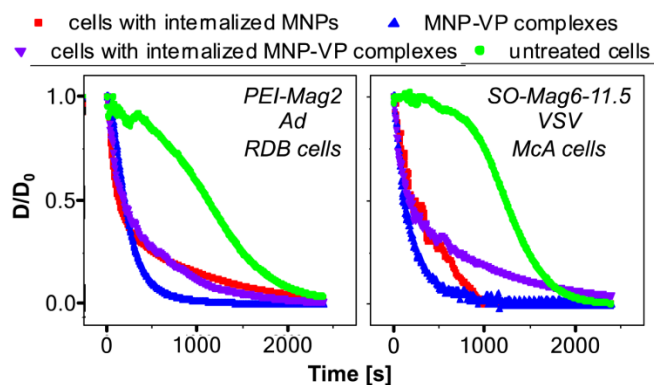


**Figure 6: Magnetophoretic mobility of magnetic viral complexes and labeled and infected cells.** Decrease of the normalized turbidity ( $D/D_0$ ) of representative suspensions of untreated cells (green), magnetic viral complexes free (blue) as well as cell internalized (purple), and cells with internalized magnetic nanoparticles (red) in an average magnetic field of  $B = 0.213 \pm 0.017$  T with a magnetic field gradient of  $\nabla B = 4 \pm 2$  T/m. The left panel shows the data set for PEI-Mag particles, Ad and RDB cells, right panel the respective data for SO-Mag particles, VSV and McA cells.

### Quantitative Magnetic Resonance Imaging (MRI)

MRI was performed to determine the MR detection limit for the non-invasive monitoring of MNP and MNP-VP complexes and to quantify the effect of cluster formation or intracellular compartmentalization on measured tissue relaxivities. The visual iron detection limit in the  $R_2^*$  maps was as low as 0.003 – 0.008 mM Fe, equaling  $0.76 \times 10^5$  labeled cells per mL at a loading of 2.5 pg iron per cell,  $0.24 \times 10^5$  labeled cells per mL at a loading of 6.7 pg iron per cell, or  $0.36 \times 10^5$  labeled cells per mL at a loading of 5.4 pg iron per cell. The MR detection limit could not be determined as all dilutions of the magnetic nanomaterial were clearly detectable above the background of mimicked liver tissue and untreated carcinoma cells, and therefore it was below 0.001 mM Fe, the lowest measured iron dilution. Figure 7 compiles image sets of exemplary phantoms with (a photograph,) a  $T_2^*$  echo image, and the corresponding  $R_2^*$  map. Figure 7A shows the phantom with homogeneously dispersed

PEI-Mag particles, panel 7B shows the phantom prepared with SO-Mag-VSV complexes internalized in McA cells and the image set 7C shows the background phantom of untreated McA cells with no detectable iron signal. The fading brown color in the photograph, the black-to-grey signal increase and the red-to-blue signal transition in the  $R_2^*$  map in all three panels mirror the decrease of magnetic material due to the dilution. Both, the  $R_2$  and the  $R_2^*$  relaxation rates linearly increased with increasing iron concentrations in the range of 0.001 to 0.34 mM Fe of free, assembled and intracellular MNPs. The measured  $R_2$  or  $R_2^*$  transverse relaxation rates and respective iron concentrations are plotted in figure 8 for the 1.5 T (8A and 8B) and 3 T (8C and 8D) data and table 5 summarizes the calculated  $r_2$  and  $r_2^*$  relaxivities, ratios of the complexed and/or internalized MNPs relative to the free MNPs, iron loading per cell and  $r_2^*/r_2$  ratios acquired on a 1.5 T clinical MRI system (corresponding 3 T data in Supplementary Material: table S2). Calculated  $r_2^*$  values were higher than  $r_2$  values and SO-Mag exhibited higher  $r_2^*$  relaxivities compared to PEI-Mag MNPs, while the  $r_2$  relaxivities were in the same range. Internalized or complexed MNPs yielded lower  $r_2$  values compared to freely dispersed MNPs. In contrast,  $r_2^*$  relaxivities increased after nanoassembly and/or cell internalization. Supplementary Material: figure S1 clearly demonstrates the comparability of data acquired either on a 1.5 T or a 3 T clinical MRI system.

### In Vivo Targeting of SO-Mag-VSV Complexes

To test targeting and non-invasive detectability of MNP-VP *in vivo*, orthotopic hepatocellular carcinoma (HCC) bearing rats were intra-tumorally injected with SO-Mag-VSV complexes in the presence of an external magnetic field. MR imaging at 24 hours post injection clearly delineated intratumoral decrease in signal intensity (figure 9A top). Regional histogram analysis quantified the signal intensity shift of SO-Mag-VSV complex-injected tumors in the lower signal range (figure 9A right). Histological analysis showed MNP-VP complex accumulation at the side of magnet placement (figure 9B). *Ex vivo* analysis revealed increased VSV titer and non-heme iron content of SO-Mag-VSV complex-injected compared to naked VSV-injected tumors (figure 9C).

noma (HCC) bearing rats were intra-tumorally injected with SO-Mag-VSV complexes in the presence of an external magnetic field. MR imaging at 24 hours post injection clearly delineated intratumoral decrease in signal intensity (figure 9A top). Regional histogram analysis quantified the signal intensity shift of SO-Mag-VSV complex-injected tumors in the lower signal range (figure 9A right). Histological analysis showed MNP-VP complex accumulation at the side of magnet placement (figure 9B). *Ex vivo* analysis revealed increased VSV titer and non-heme iron content of SO-Mag-VSV complex-injected compared to naked VSV-injected tumors (figure 9C).

### Discussion

This work reports on the physico-chemical and imaging characteristics of selected magnetic nanoparticles (MNPs) and derived complexes of these MNPs with adenovirus (Ad) and vesicular stomatitis virus (VSV). PEI-Mag2 and SO-Mag6-11.5 particles possessed highly positive electrokinetic potential, enabling self-assembly based on electrostatic interaction of negatively charged viral particles (VPs) and positively charged MNPs. Transmission electron microscopy (TEM) was used to visualize complex and cluster formation of free magnetic material and upon cellular uptake. Quantitative magnet resonance imaging (MRI) of gel phantoms revealed decreased  $r_2$  and increased  $r_2^*$  values upon complexation and clusterization. First *in vivo* application of VSV-based MNP-VP complexes demonstrated their targeting and imaging properties.

Sample	PEI-Mag2					SO-Mag6-11.5				
	$r_2$ [mM <sup>-1</sup> Fe s <sup>-1</sup> ]	ratio [%]	$r_2^*$ [mM <sup>-1</sup> Fe s <sup>-1</sup> ]	ratio [%]	$r_2^*/r_2$	$r_2$ [mM <sup>-1</sup> Fe s <sup>-1</sup> ]	ratio [%]	$r_2^*$ [mM <sup>-1</sup> Fe s <sup>-1</sup> ]	ratio [%]	$r_2^*/r_2$
MNP	215 ± 9	100	441 ± 20	100	2.1	286 ± 7	100	851 ± 13	100	3.0
MNP in McA	45 ± 4 (4.5 pg Fe/cell)	21	585 ± 15 (4.5 pg Fe/cell)	133	13.0	30 ± 2 (5.4 pg Fe/cell)	10	787 ± 14 (5.4 pg Fe/cell)	92	26.2
MNP-VSV	45 ± 7	21	541 ± 23	123	12.0	32 ± 4	11	1030 ± 32	121	32.2
MNP-VSV in McA	18 ± 3 (3.2 pg Fe/cell)	8	595 ± 7 (3.2 pg Fe/cell)	135	33.1	55 ± 2 (2.5 pg Fe/cell)	19	1450 ± 57 (2.5 pg Fe/cell)	170	26.4
MNP in RDB	17 ± 1 (17.3 pg Fe/cell)	8	546 ± 37 (17.3 pg Fe/cell)	124	32.1	36 ± 1 (15.9 pg Fe/cell)	13	1209 ± 136 (15.9 pg Fe/cell)	142	33.6
MNP-Ad	115 ± 10	53	503 ± 11	114	4.4	18 ± 2	6	1020 ± 31	120	56.7
MNP-Ad in RDB	28 ± 5 (6.7 pg Fe/cell)	13	801 ± 23 (6.7 pg Fe/cell)	182	28.6	10 ± 6 (7.4 pg Fe/cell)	3	442 ± 17 (7.4 pg Fe/cell)	52	44.2

**Table 5:  $r_2$  and  $r_2^*$  relaxivities of the MNP assemblies.** The table shows the  $r_2$  and  $r_2^*$  relaxivity data of the free MNPs and MNP-VP complex assemblies in liver-mimicking agarose phantoms, and the ratios of the nanoassembly relaxivity normalized to the relaxivity of free MNPs ( $r_2/r_2(\text{MNP})$  and  $r_2^*/r_2^*(\text{MNP})$ , respectively, green) and the  $r_2^*/r_2$  ratios (red). All measurements were performed using a clinical 1.5 T MRI system from Philips.

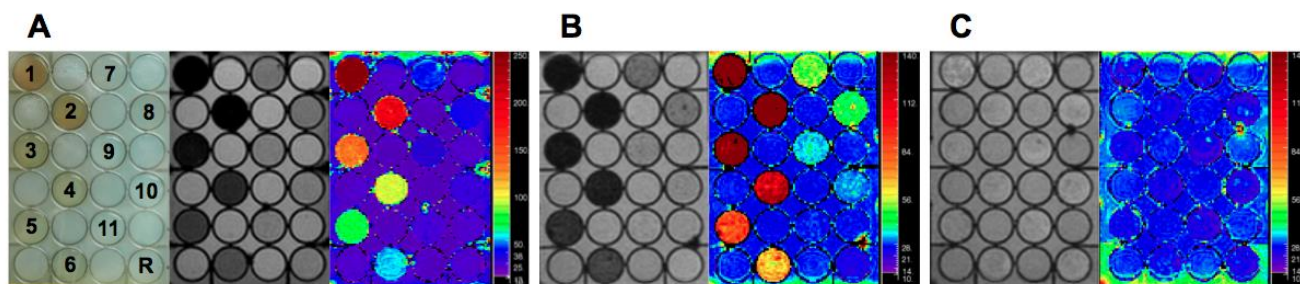


**Figure 7: Magnet resonance imaging of exemplary liver-mimicking phantoms.** Panels show (from left to right) a photograph of the phantom, a  $T_2^*$  echo image, and the respective  $R_2^*$  map. **A** PEI-Mag2, **B** SO-Mag-VSV-complexes in McA cells, **C** untreated McA cells. All phantoms were prepared from a 2-to-3 dilution series of the magnetic nanomaterial in the wells 1-11 and reference material in well R.

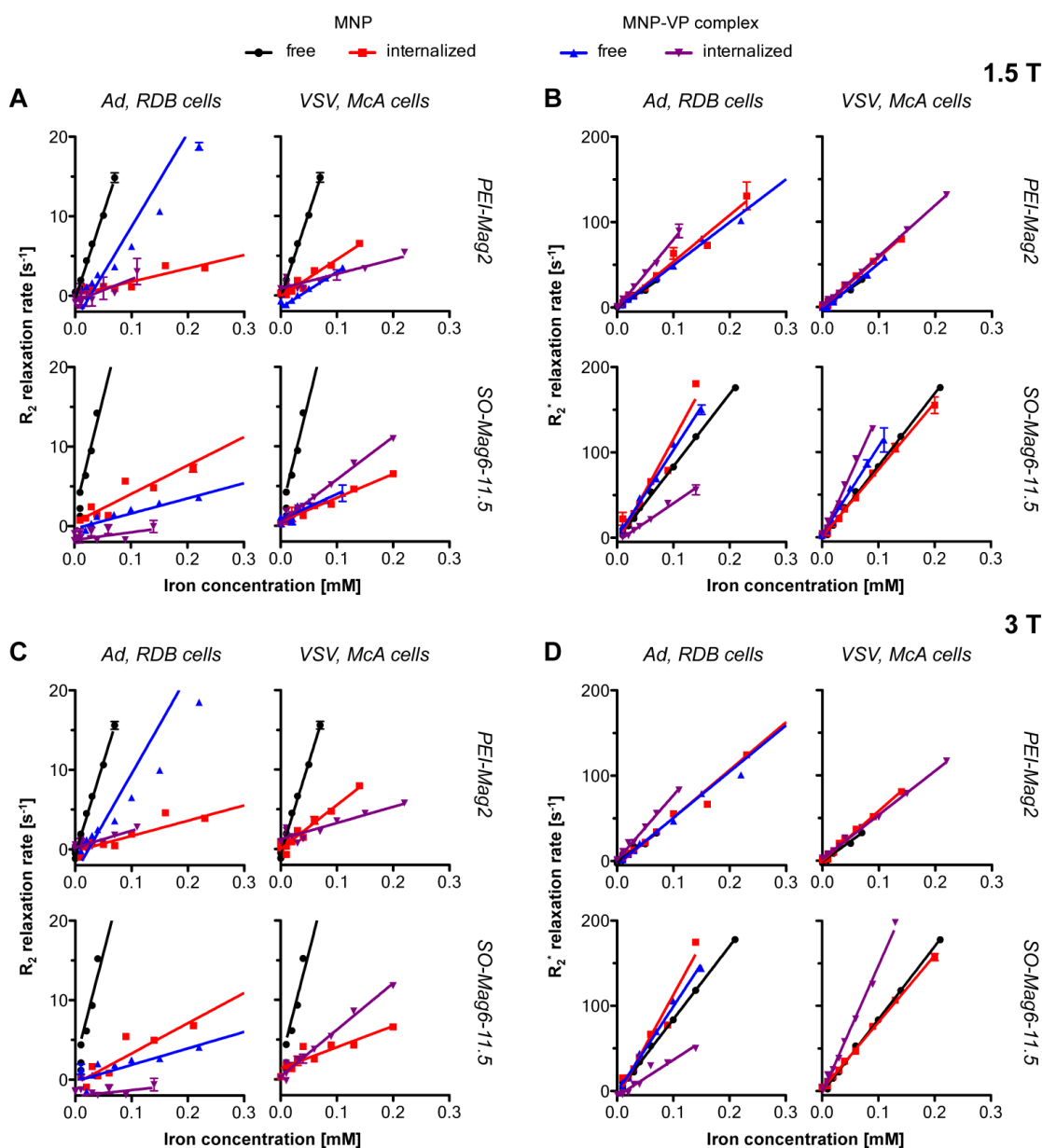


**Figure 8:  $r_2$  and  $r_2^*$  relaxivity plots.** In the panels **A** and **C** transverse relaxation rate  $R_2$ , in the panels **B** and **D** the spin-spin relaxation rate  $R_2^*$  are each plotted against the respective iron concentrations. The data of panels **A** and **B** were acquired at 1.5 T, the data of panels **C** and **D** show the corresponding data acquired at 3 T, both on clinical MRI systems. In each panel, the left graphs show the data for Ad and RDB cells, the right graphs the data for VSV and McA cells, the top graphs show the datasets for PEI-Mag particles and the bottom graphs for SO-Mag particles. Free MNPs are plotted in black, cell internalized MNPs in red, and free complexes in blue and cell internalized complexes in purple.

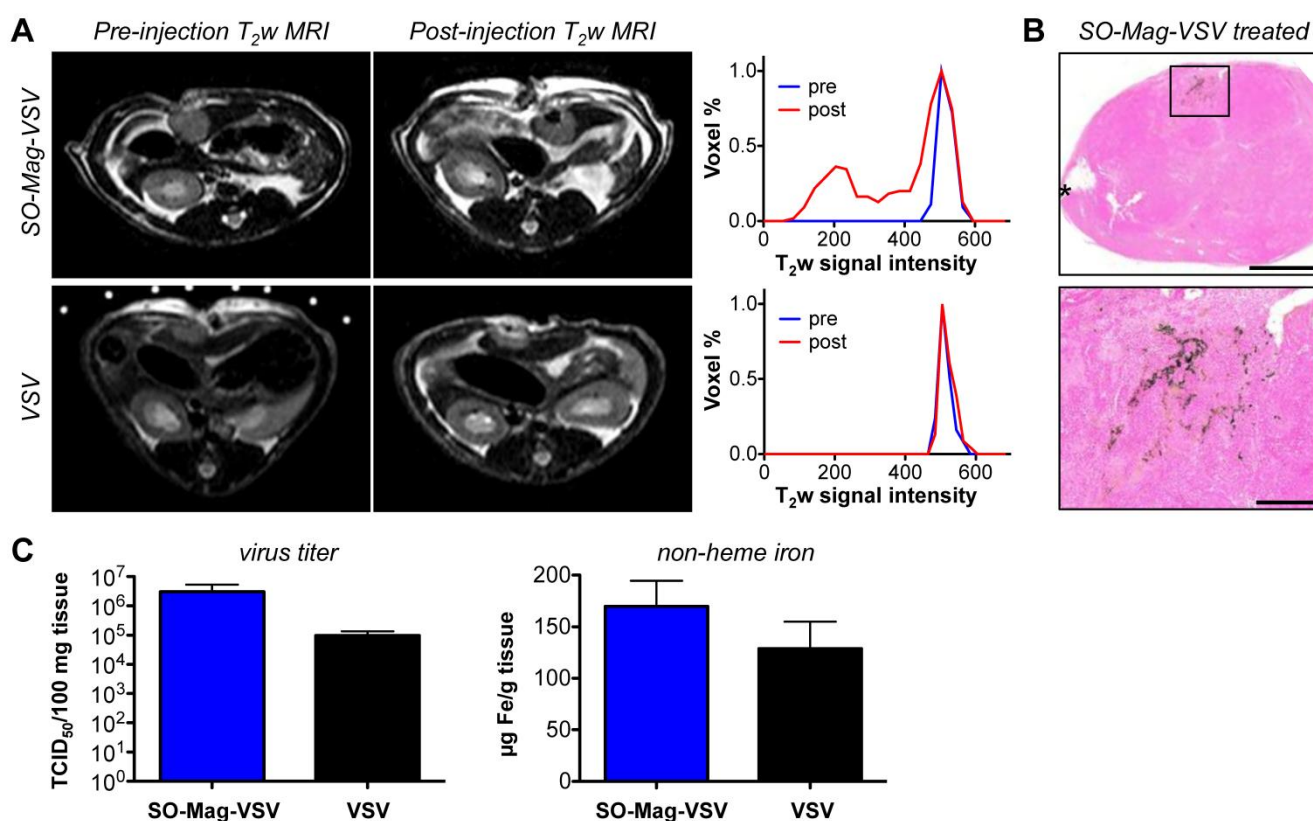


**Figure 9:** *In vivo* targeting of SO-Mag-VSV complexes. **A** Pre- and 24 hour post-injection T<sub>2</sub>-weighted MR images of orthotopic HCC after SO-Mag-VSV complex (top row) or naked VSV (bottom row) injection. The corresponding histograms (A, right) illustrate the signal loss after magnetic complex application in an emerging signal shoulder in the lower signal range. **B** Overview (top) and high magnification micrographs of prussian blue staining 24 hours after SO-Mag-VSV complex injection. The asterisk marks the injection site and the magnet was placed above the boxed area (top); scale bars 2,000 µm (top) and 500 µm (bottom), respectively. **C** Intra-tumoral virus titer and non-heme iron of whole tumors sampled 30 minutes post infection with SO-Mag-VSV complexes (n=4, blue) and naked VSV (n=3, black).

The differences in the mean hydrodynamic diameters of the selected MNPs resulted from the differences in the magnetic moments of the cores, the electrokinetic potentials and the surface compositions. The PEI-Mag particles had a small average hydrodynamic diameter representative of single particles in the aqueous suspension, whereas the SO-Mag particles had a larger average hydrodynamic diameter in aqueous suspensions indicating that the particles tend to aggregate into small assemblies due to increased magnetic dipole-dipole interactions [29, 31]. The average hydrodynamic diameter of the primary non-aggregated core nanoparticle without PEI-modification was  $D_h = 40 \pm 14$  nm in water [12]. The selected MNPs both comprised branched PEI<sub>Br-25</sub> in their coating and were therefore highly positively charged. Such PEI-stabilized particles display high cell labeling efficiencies and were suitable for association with negatively charged VPs into efficient complexes at virus-specific and virus-optimized iron-to-virus ratios resulting in high magnetotransduction efficacy. The self-assembly was of predominantly electrostatic nature and stable MNP-VP complexes formed. Such self-assembly is known to modify

the magnetic behavior relative to that of isolated particles and happens often in liquid medium [50]. The physico-chemical properties of the MNP-Ad complexes were consistent with earlier studies on such complexes [29, 31] and the MNP-VSV complexes were within the same range. In the MNP-VP complexes, the MNPs were most probably arranged in layers around the VPs due to predominantly electrostatic interactions between the negatively charged virus and the positively charged particles and magnetic dipole-dipole interaction between the magnetic particles.

Both MNPs and MNP-VP complexes displayed high cell labeling and infection efficiencies with the magnetofection method applied [37]. The efficiency of magnetic cell labeling with and without an externally applied magnetic field was previously tested in RDB cells [29, 31] and McA cells [12] and we were able to reach even higher labeling efficiencies. The labeling was between 2.5 and 5.4 pg Fe/cell in McA cells and 6.7 and 17.3 pg Fe/cell in RDB cells after application of 10 and 25 pg Fe/cell, respectively, indicating that the labeling efficiencies ranged between 25 % and 69 %.

The localization and aggregation state of MNPs and MNP-VP complexes after cell internalization as well as their appearance in suspended form was elucidated by transmission electron microscopy. On the TEM photomicrographs of free MNPs and magnetic viral complexes, both samples were more or less dispersed, and single self-assembled complexes could easily be identified. The cell-internalized viral complexes were encapsulated in endosomes, whereas the free particles were mostly clustered within the cytoplasm and only in very few endosomes. Cytoplasmic localization [51, 52] and endosomal encapsulation [53] of the internalized MNPs was also observed in other experiments with MNP-labeled cells. We assume that the compartmentalization, clusterization and distribution of MNPs and MNP-VP complexes in cells depended on the uptake mechanism. From the TEM photomicrographs we speculate that the uptake of viral complexes was not receptor mediated, and therefore, cell-bound complexes were most probably endocytosed. Whereas free MNPs might be directly taken up into the cytoplasm and aggregated there. In earlier studies, cell uptake and transfection with enclosed plasmid DNA of magnetic lipoplexes was very efficient. The sizes of these lipoplexes were comparable to our complexes. Even lipoplexes of about 2 micron were efficiently internalized [54]. Other groups found a larger complex size advantageous to good internalization and transfection [55-57]. In contrast to the cytoplasmic localization of MNPs in our study, others found iron oxide particles to be localized intracellularly primarily in the tubular lysosomal compartment [58, 59]. Sun *et al.* identified the non-facilitated endocytosis of small particles into human hepatocellular liver carcinoma cells from TEM images [60]. Chemically modified dextran-coated iron oxides were internalized through receptor-mediated endocytosis into highly specialized cells such as hepatocytes [61, 62] or pancreatic acinar cells [63].

*In vitro* infection experiments have shown that exposure of the MNP-virus complexes to 50 % FCS resulted in considerable inhibition of the oncolytic activity of the naked virus both for VSV and Ad vectors. In contrast, oncolytic potency was considerably improved due to assembling with selected MNPs at optimal iron-to-virus ratios and remained high even at high serum concentration for the complexes with both VSV and Ad (table 3 and figure 5). The corona from multiple magnetic nanoparticles surrounding a viral particle was previously shown to ensure a defense against virus neutralizing antibodies [29]. The magnetic complexes of Ad were also shown to be relatively stable with respect to disintegration at high serum concentrations [12]. These findings promise enhancement of oncolytic potency due to assembling

with MNPs, especially under application of the magnetic field, as it was shown in *in vivo* experiments on local application of the magnetic complexes of the oncolytic adenovirus in a murine tumor model [29].

In addition to their physico-chemical properties such as hydrodynamic diameter and electrokinetic potential, the selected core-shell MNPs and their optimized self-assembled complexes with virus particles were characterized for their magnetic responsiveness in applied magnetic fields [45, 46]. Therefore, the turbidity clearance curves were plotted and extrapolated to calculate the magnetophoretic mobility and the number of associated MNPs per virus particle applying Wilhelm *et al.*'s method [64]. The results were comparable to previous studies on MNP-VP complexes [29, 31].

From earlier studies we knew that the selected core-shell type SO-Mag MNPs showed excellent  $r_2$  and  $r_2^*$  relaxivities, both free and cell-internalized [12]. To further determine the efficacy of free and cell-internalized MNP-VP complexes as contrast agents for MRI and to identify the detection limit of iron in the different assemblies, tissue-mimicking MRI phantoms with homogeneously distributed nanomaterial were prepared. Although Kuhlperter *et al.* found no difference in the  $R_2$  and  $R_2^*$  effect for highly iron-loaded cells in a lower number and low-loaded cells in a higher number with comparable average iron concentrations per sample [65], we decided to use comparable iron loadings and cell numbers per concentration. Therefore, in our phantoms cells with similar iron loadings and the respective amounts of free MNPs and complexes were diluted and homogeneously distributed and embedded in the agarose gel phantoms to identify the detection limit. The linear increase of the  $R_2$  and  $R_2^*$  relaxation rates with increasing iron concentrations is in concordance with previous findings for iron oxides [12, 13, 66, 67]. The chosen tissue for the baseline relaxation [65] was liver, as HCC and pancreatic adenocarcinoma, which are the tumor origins of our model cell lines, both develop liver pathologies. Thereby, transferability of the *in vitro* iron quantification data to *in vivo* studies could be assured.

The assembly of MNP-VP complexes and further cell internalization led to about 47 - 97 % reduction of  $r_2$  and 14 - 82 % increase of  $r_2^*$  after internalization compared to free particles, which both yielded the highest  $r_2$  and lower  $r_2^*$  relaxivities. Cell internalization of free particles reduced the  $r_2$  relaxivities by 79 - 92 %, while the internalization of the corresponding MNP-VP complexes reduced the  $r_2$  relaxivity in the same range (79 - 94 %), with the exception of the PEI-Mag-Ad complexes (47 %). Perez *et al.* also found the  $T_2$  signal intensity to decrease in reaction to

nanoassembly formation between herpes simplex or adenovirus particles and MNPs labeled with virus-specific antibodies [68, 69]. Others, too, saw reduced  $r_2$  relaxation rates relative to free particles induced by the intracellular iron particle clusterization [51-53, 65, 70, 71]. In general, our  $r_2$  relaxivities of 10 to 286  $\text{mM}^{-1} \text{Fe s}^{-1}$  were within the range or even better than those of clinically used contrast agents that range between 10 – 100  $\text{mM}^{-1} \text{Fe s}^{-1}$  [72]. Shapiro et al. also found significantly reduced  $r_2$  relaxivities and amplified  $r_2^*$  relaxivities after aggregation [72]. Similarly, Kuhlperter et al. observed the same relaxivity pattern after cell-binding of MNPs [65], always compared to the relaxivities of the respective free MNPs. In general, the  $r_2^*$  relaxivities were higher than the  $r_2$  relaxivities. The  $r_2^*$  to  $r_2$  ratio after particle assembly and/or cell internalization compared to free, suspended particles was dramatically increased as reported by others [71]. The variation was 2- to 33-fold for PEI-Mag and 3- to 56-fold for SO-Mag samples. These variations could be explained by the restricted diffusion of water-protons. The lower  $r_2$  relaxivities were in concordance with the motional narrowing effect [73], the effect of restricted water/proton diffusion after compartmentalization [70] and reduced proton relaxation [53]. It was induced by the clusterization of MNPs around virus particles and intracellular compartmentalization. The increased diffusion distance of protons along intracellularly clustered magnetic particles decreased the  $r_2$  relaxivities and increased the  $r_2^*$  relaxivities. In addition, the relatively small field inhomogeneities induced by small free MNPs in the nm range are potentiated in clustered particles of virus complexes and intracellular aggregates that occur in the high nm or  $\mu\text{m}$  range. Both factors lead to incoherent spin dephasing and the outer-sphere relaxation theory could be applied to explain the  $r_2$  relaxivity drop [51]. The static dephasing regime theory says that large compartmental magnetic moments produce a strong enough outer-sphere dipolar field so that diffusion has a minimal effect on the MR signal decay and this decay is unaffected by details of the compact magnetic aggregate shape [71, 74]. Hence the aggregation state directly modulated the intracellular relaxivity of the cell and complex samples in comparison to free MNPs dispersed in agarose gel. Therefore  $r_2$  is influenced by the concentration and the assembly state of the MNPs,  $r_2^*$  is mainly sensitive towards the iron concentration and so  $R_2^*$ -weighted acquisition was assumed to be the potentially most sensitive method to identify the presence of iron-oxide particles and labeled cells [65, 71]. Therefore, the increased  $r_2^*$  relaxivity of MNP-VP complexes should further enhance the non-invasive detectability by MRI. Differences in  $R_2^*$  and  $r_2^*$  be-

tween the two particles could be explained by  $D_H$ -dependent higher diffusion restriction in SO-Mag MNPs as they tend to aggregate, even in their already dispersed state.

In our *in vitro* liver mimicking phantoms, iron concentrations as low as approximately 0.003 – 0.008 mM Fe in about  $10^5$  labeled cells/mL agarose were visually detectable above the liver background with sufficient image contrast. That detection limit was more sensitive than our previous result of 0.025 mM Fe for the SO-Mag particles [12], 0.021 mM Fe for NDT-Mag1 particles [13] or the detection limits of other groups with of  $10^6$  Endorem<sup>®</sup>-labeled cells per mL gelatin on a 3 T clinical MRI system at comparable cell iron loading concentrations of 25 pg Fe/cell, so 0.448 mM iron [75], and was within the same range as Weissleder et al. with 0.002 mM Fe in evenly distributed ( $5 \times 10^6$  cells/mL) or pelleted cells ( $10^5$  in 20  $\mu\text{L}$ ) in 2 % agarose gel on a 1.5 T MRI system [59]. The determined relaxivities were also comparable to literature values; for example the  $r_2$  relaxivity of virus-complex-labeled McA cells with 2.5 pg Fe/cell was 55  $\text{mM}^{-1} \text{Fe s}^{-1}$  (at 1.5 T), and Estapor<sup>®</sup> labeled neutrophils with 2 pg Fe/cell had a  $r_2$  of 74  $\text{mM}^{-1} \text{Fe s}^{-1}$  (at 4.0 T) [76].

In future *in vivo* studies, in particular on viral cancer therapy, such tissue-mimicking phantoms could be applied for the non-invasive quantification of exogenic iron from magnetic nanoassemblies in animal tissue by MRI. The calibration should be performed using phantoms prepared from cells with internalized complexes rather than from complexes alone or free particles. Besides the application for direct tracking of viral vectors to their target tissues, MNP-labeled cells, such as muscle stem cells [77] and monocyte macrophages [78], could also be monitored *in vivo*. In another study magnetophages, bacteriophages with USPIOs coupled to their wall, were used to identify apoptotic areas in the liver [79]. De Vries et al. even found the magnetic labeling and subsequent MR imaging of the labeled cells more sensitive than the radioactive labeling and subsequent scintigraphy of the same cells in *ex vivo* scans of the lymph node of a dendritic cell-treated melanoma patient [80].

With our proof-of-principle study we could prove the *in vivo* applicability of the magnetic viral complexes. HCC liver lesion bearing Buffalo rats were injected with either naked VSV or SO-Mag-VSV complexes and after 30 minutes of magnetic targeting the virus titer in virus complex treated animals was higher than the titers in animals treated with naked virus. 24 hours after infection there was still a clearly detectable iron-induced MRI signal loss in the tumor lesions of SO-Mag-VSV complex treated animals,

whereas the VSV-treated control animal showed no signal change in their tumors.

## Conclusion

Both selected core-shell type MNPs were characterized by high  $r_2$  and  $r_2^*$  relaxivities. The assembly of these MNPs with VPs and cell internalization of MNPs and MNP-VP complexes resulted in the reduction of  $r_2$  and the increase of  $r_2^*$  compared to free MNPs. This was likely due to the motional narrowing effect after intracellular clusterization of the particles and complexes, respectively. The low visual iron detection limit of about 0.003 - 0.008 mM Fe and the MRI detection limit below 0.001 mM Fe are a good basis for direct quantification of the targeting efficacy of MNP-VP complexes *in vivo* and *ex vivo*. Here, our tissue-mimicking phantoms with cell-internalized MNP-VP complexes could serve for calibration. Our results on the *in vivo* application of the VSV based MNP-VPs are promising as intra-tumoral iron accumulation could clearly be visualized by MRI and the MNP-VP complexes led to higher intra-tumoral virus titers compared to naked virus.

## Abbreviations

Ad: adenovirus; ddH<sub>2</sub>O: double distilled water; DNA: deoxyribonucleic acid; Dh: hydrodynamic diameter; HCC: hepatocellular carcinoma; MF: magnetic field; MNP: magnetic nanoparticle; MRI: magnet resonance imaging; OD: optical density; PBS: phosphate buffered saline; PEI: polyethylenimine; RNA: ribonucleic acid; SPIO: superparamagnetic iron oxide; TEM: transmission electron microscopy; USPIO: ultrasmall paramagnetic iron oxide; VP: virus particle; VSV: vesicular stomatitis virus.

## Supplementary Material

Tables S1 and S2, Figure S1.  
<http://www.thno.org/v05p0667s1.pdf>

## Acknowledgments

This project has been financially supported by the German Research Foundation (DFG) within the SFB-Initiative 824 (collaborative research center), "Imaging for Selection, Monitoring and Individualization of Cancer Therapies" (project C6 to R.B. and project Z2 to A.W.), by the German Federal Ministry of Education (BMBF) within the German Excellence Cluster  $m^4$  to E.J.R. and R.B., and by the DFG Research Unit FOR917 (Project PL 281/3-1), the NIM (Nanosystems Initiative Munich), the BMBF Project ELA 10/002 and through the ZIM cooperation project STEP-MAG to O.M.

## Author Contributions

Conceived and designed the experiments: I.A., O.M., J.A., R.B.

Performed the experiments: I.A., O.M., J.A., M.A.  
 Analyzed the data: I.A., O.M., M.S., M.A., R.B.

Contributed reagents/materials/analysis tools: I.A., O.M., M.S., J.A., M.A., C.P., O.E., A.W., E.R., R.B.

Wrote the manuscript: I.A., O.M., R.B.

## Competing Interests

The authors have declared that no competing interest exists.

## References

- Wang C, Zhang H, Chen B, Yin H, Wang W. Study of the enhanced anticancer efficacy of gambogic acid on Capan-1 pancreatic cancer cells when mediated via magnetic Fe<sub>3</sub>O<sub>4</sub> nanoparticles. *Int J Nanomedicine*. 2011; 6: 1929-35. doi:10.2147/IJN.S24707.
- Child HW, del Pino PA, De La Fuente JM, Hursthouse AS, Stirling D, Mullen M, et al. Working together- the combined application of a magnetic field and penetratin for the delivery of magnetic nanoparticles to cells in 3D. *ACS Nano*. 2011; 5: 7910-9.
- Levy M, Luciani N, Alloeyau D, Elgrabli D, Deveaux V, Pechoux C, et al. Long term in vivo biotransformation of iron oxide nanoparticles. *Biomaterials*. 2011; 32: 3988-99. doi:10.1016/j.biomaterials.2011.02.031.
- Santra S, Kaitanis C, Grimm J, Perez J. Drug/dye-loaded, multifunctional iron oxide nanoparticles for combined targeted cancer therapy and dual optical/magnetic resonance imaging. *Small*. 2009; 5: 1862-8. doi:10.1002/smll.200900389.
- Yallapu M, Othman S, Curtis E, Gupta B, Jaggi M, Chauhan S. Multi-functional magnetic nanoparticles for magnetic resonance imaging and cancer therapy. *Biomaterials*. 2011; 32: 1890-905. doi:10.1016/j.biomaterials.2010.11.028.
- Cole A, Yang V, David A. Cancer theranostics: the rise of targeted magnetic nanoparticles. *Trends Biotechnol*. 2011; 29: 323-32. doi:10.1016/j.tibtech.2011.03.001.
- Cole A, David A, Wang J, Galban C, Yang V. Magnetic brain tumor targeting and biodistribution of long-circulating PEG-modified, cross-linked starch-coated iron oxide nanoparticles. *Biomaterials*. 2011; 32: 6291-301. doi:10.1016/j.biomaterials.2011.05.024.
- Cole A, David A, Wang J, Galban C, Hill H, Yang V. Polyethylene glycol modified, cross-linked starch-coated iron oxide nanoparticles for enhanced magnetic tumor targeting. *Biomaterials*. 2011; 32: 2183-93. doi:10.1016/j.biomaterials.2010.11.040.
- Kettering M, Richter H, Wiekhorst F, Bremer-Streck S, Trahms L, Kaiser W, et al. Minimal-invasive magnetic heating of tumors does not alter intra-tumoral nanoparticle accumulation, allowing for repeated therapy sessions: an in vivo study in mice. *Nanotechnology*. 2011; 22: 505102. doi:10.1088/0957-4484/22/50/505102.
- Giustini A, Ivkov R, Hoopes P. Magnetic nanoparticle biodistribution following intratumoral administration. *Nanotechnology*. 2011; 22: 345101. doi:10.1088/0957-4484/22/34/345101.
- Dennis C, Jackson A, Borchers J, Hoopes P, Strawbridge R, Foreman A, et al. Nearly complete regression of tumors via collective behavior of magnetic nanoparticles in hyperthermia. *Nanotechnology*. 2009; 20: 395103. doi:10.1088/0957-4484/20/39/395103.
- Mykhaylyk O, Sobisch T, Almstätter I, Sanchez-Antequera Y, Brandt S, Anton M, et al. Silica-iron oxide magnetic nanoparticles modified for gene delivery: a search for optimum and quantitative criteria. *Pharm Res*. 2012; 29: 1344-65. doi:10.1007/s11095-011-0661-9.
- Mykhaylyk O, Steingötter A, Perea H, Aigner J, Botnar R, Plank C. Nucleic Acid Delivery to Magnetically-Labeled Cells in a 2D Array and at the Luminal Surface of Cell Culture Tube and Their Detection by MRI. *Journal of Biomedical Nanotechnology*. 2009; 5: 692-706. doi:10.1166/jbn.2009.1086.
- Chanana M, Mao Z, Wang D. Using Polymers to Make Up Magnetic Nanoparticles for Biomedicine. *Journal of Biomedical Nanotechnology*. 2009; 5: 652-68. doi:10.1166/jbn.2009.1082.
- Zhang C, Wängler B, Morgenstern B, Zentgraf H, Eisenhut M, Untenecker H, et al. Silica- and alkoxysilane-coated ultrasmall superparamagnetic iron oxide particles: a promising tool to label cells for magnetic resonance imaging. *Langmuir*. 2007; 23: 1427-34.
- Strijkers GJ, Mulder WJ, van Tilborg GA, Nicolay K. MRI contrast agents: current status and future perspectives. *Anticancer Agents Med Chem*. 2007; 7: 291-305.
- Carr D. The use of iron and gadolinium chelates as NMR contrast agents: animal and human studies. *Physiol Chem Phys Med NMR* 1984; 16: 137-44.

18. Campbell S, Gromeier M. Oncolytic viruses for cancer therapy I. Cell-external factors: virus entry and receptor interaction. *Onkologie*. 2005; 28: 144-9.
19. Davis J, Fang B. Oncolytic virotherapy for cancer treatment: challenges and solutions. *J Gene Med*. 2005; 7: 1380-9. doi:10.1002/jgm.800.
20. Liu T, Galanis E, Kirn D. Clinical trial results with oncolytic virotherapy: a century of promise, a decade of progress. *Nat Clin Pract Oncol*. 2007; 4: 101-17. doi:10.1038/nponc0736.
21. Schellingerhout D, Bogdanov AJ. Viral imaging in gene therapy noninvasive demonstration of gene delivery and expression. *Neuroimaging Clin N Am*. 2002; 12: 571-81.
22. Meerani S, Yao Y. Oncolytic Viruses in Cancer Therapy. *European Journal of Scientific Research*. 2010; 40: 156-71.
23. Khuri F, Nemunaitis J, Ganly I, Arseneau J, Tannock I, Romel L, et al. A controlled trial of intratumoral ONYX-015, a selectively-replicating adenovirus, in combination with cisplatin and 5-fluorouracil in patients with recurrent head and neck cancer. *Nat Med*. 2000; 6: 879-85.
24. Sapet C, Pellegrino C, Laurent N, Sicard F, Zelphati O. Magnetic nanoparticles enhance adenovirus transduction in vitro and in vivo. *Pharm Res*. 2012; 29: 1203-18. doi:10.1007/s11095-011-0629-9.
25. Shinozaki K, Ebert O, Kournioti C, Tai Y, Woo S. Oncolysis of multifocal hepatocellular carcinoma in the rat liver by hepatic artery infusion of vesicular stomatitis virus. *Mol Ther*. 2004; 9: 368-76. doi:10.1016/j.yjmt.2003.12.004.
26. Altomonte J, Braren R, Schulz S, Marozin S, Rummeny E, Schmid R, et al. Synergistic antitumor effects of transarterial viroembolization for multifocal hepatocellular carcinoma in rats. *Hepatology*. 2008; 48: 1864-73. doi:10.1002/hep.22546.
27. Wenzel D, Rieck S, Vosen S, Mykhaylyk O, Trueck C, Eberbeck D, et al. Identification of magnetic nanoparticles for combined positioning and lentiviral transduction of endothelial cells. *Pharm Res*. 2012; 29: 1242-54. doi:10.1007/s11095-011-0657-5.
28. Trueck C, Zimmermann K, Mykhaylyk O, Anton M, Vosen S, Wenzel D, et al. Optimization of magnetic nanoparticle-assisted lentiviral gene transfer. *Pharm Res*. 2012; 29: 1255-69. doi:10.1007/s11095-011-0660-x.
29. Tresilwised N, Pithayanukul P, Holm P, Schillinger U, Plank C, Mykhaylyk O. Effects of nanoparticle coatings on the activity of oncolytic adenovirus-magnetic nanoparticle complexes. *Biomaterials*. 2012; 33: 256-69. doi:10.1016/j.biomaterials.2011.09.028.
30. Mannell H, Pircher J, Räthel T, Schilberg K, Zimmermann K, Pfeifer A, et al. Targeted endothelial gene delivery by ultrasonic destruction of magnetic microbubbles carrying lentiviral vectors. *Pharm Res*. 2012; 29: 1282-94. doi:10.1007/s11095-012-0678-8.
31. Tresilwised N, Pithayanukul P, Mykhaylyk O, Holm PS, Holzmüller R, Anton M, et al. Boosting oncolytic adenovirus potency with magnetic nanoparticles and magnetic force. *Mol Pharm*. 2010; 7: 1069-89.
32. Hofmann A, Wenzel D, Becher U, Freitag D, Klein A, Eberbeck D, et al. Combined targeting of lentiviral vectors and positioning of transduced cells by magnetic nanoparticles. *Proc Natl Acad Sci U S A*. 2009; 106: 44-9. doi:10.1073/pnas.0803746106.
33. Plank C, Zelphati O, Mykhaylyk O. Magnetically enhanced nucleic acid delivery. Ten years of magnetofection-Progress and prospects. *Adv Drug Deliv Rev*. 2011; 63: 1300-31. doi:10.1016/j.addr.2011.08.002.
34. Trueck C, Zimmermann K, Mykhaylyk O, Anton M, Vosen S, Wenzel D, et al. Optimization of Magnetic Nanoparticle-Assisted Lentiviral Gene Transfer. *Pharm Res*. 2012. doi:10.1007/s11095-011-0660-x.
35. Tresilwised N, Pithayanukul P, Mykhaylyk O, Holm PS, Holzmüller R, Anton M, et al. Boosting Oncolytic Adenovirus Potency with Magnetic Nanoparticles and Magnetic Force. *Molecular Pharmaceutics*. 2010; 7: 1069-89. doi:10.1021/mp100123t.
36. Raty JK, Liimatainen T, Wirth T, Airenen KJ, Ihalainen TO, Huhtala T, et al. Magnetic resonance imaging of viral particle biodistribution in vivo. *Gene Ther*. 2006; 13: 1440-6. doi:10.1038/sj.gt.3302828.
37. Mykhaylyk O, Sanchez-Antequera Y, Vlaskou D, Plank C. Generation of magnetic nonviral gene transfer agents and magnetofection in vitro. *Nat Protoc*. 2007; 2: 2391-411. doi:10.1038/nprot.2007.352.
38. Mykhaylyk O, Sobisch T, Almstatter I, Sanchez-Antequera Y, Brandt S, Anton M, et al. Silica-Iron Oxide Magnetic Nanoparticles Modified for Gene Delivery: A Search for Optimum and Quantitative Criteria. *Pharm Res*. 2012. doi:10.1007/s11095-011-0661-9.
39. Kowalski JB, Tallentire A. Substantiation of 25 kGy as a sterilization dose: a rational approach to establishing verification dose. *Radiat Phys Chem*. 1999; 54: 55-64.
40. Krill CE, Birringer R. Estimating grain-size distributions in nanocrystalline materials from X-ray diffraction profile analysis. *Philos Mag A*. 1998; 77: 621-40.
41. Holm PS, Lage H, Bergmann S, Jurchott K, Glockzin G, Bernshausen A, et al. Multidrug-resistant cancer cells facilitate E1-independent adenoviral replication: impact for cancer gene therapy. *Cancer Res*. 2004; 64: 322-8.
42. Mittereder N, March KL, Trapnell BC. Evaluation of the concentration and bioactivity of adenovirus vectors for gene therapy. *J Virol*. 1996; 70: 7498-509.
43. Torrance JD, Bothwell TH. Tissue iron stores. In: JD C, editor. *Methods in hematology: iron*. New York: Churchill Livingstone. 1981: 90-115.
44. Dalton A. A chrome-osmium fixative for electron microscopy. *Anat Rec*. 1973.
45. Mykhaylyk O, Zelphati O, Rosenecker J, Plank C. siRNA delivery by magnetofection. *Curr Opin Mol Ther*. 2008; 10: 493-505.
46. Mykhaylyk O, Zelphati O, Hammerschmid E, Anton M, Rosenecker J, Plank C. Recent advances in magnetofection and its potential to deliver siRNAs in vitro. *Methods Mol Biol*. 2009; 487: 111-46.
47. Christoffersson J, Olsson L, Sjöberg S. Nickel-Doped Agarose Gel Phantoms in MR Imaging. *Acta Radiologica*. 1991; 32: 426-31.
48. Dahnke H, Schaeffter T. Limits of detection of SPIO at 3.0 T using T2 relaxometry. *Magn Reson Med*. 2005; 53: 1202-6. doi:10.1002/mrm.20435.
49. Mykhaylyk O, Vlaskou D, Tresilwised N, Pithayanukul P, Moller W, Plank C. Magnetic nanoparticle formulations for DNA and siRNA delivery. *Journal of Magnetism and Magnetic Materials*. 2007; 311: 275-81.
50. Majetch S, Wen T, Booth R. Functional magnetic nanoparticle assemblies: formation, collective behavior, and future directions. *ACS Nano*. 2011; 5: 6081-4.
51. Klug G, Kampf T, Bloemer S, Bremicker J, Ziener C, Heymer A, et al. Intracellular and extracellular T1 and T2 relaxivities of magneto-optical nanoparticles at experimental high fields. *Magn Reson Med*. 2010; 64: 1607-15. doi:10.1002/mrm.22557.
52. Rogers W, Meyer C, Kramer C. Technology insight: in vivo cell tracking by use of MRI. *Nat Clin Pract Cardiovasc Med*. 2006; 3: 554-62. doi:10.1038/ncpcardio0659.
53. Billotey C, Wilhelm C, Devaud M, Bacri J, Bittoun J, Gazeau F. Cell internalization of anionic maghemite nanoparticles: quantitative effect on magnetic resonance imaging. *Magn Reson Med*. 2003; 49: 646-54. doi:10.1002/mrm.10418.
54. Sanchez-Antequera Y, Mykhaylyk O, Thalhammer S, Plank C. Gene delivery to Jurkat T cells using non-viral vectors associated with magnetic nanoparticles. *Int J Biomed Nanosci Nanotech*. 2010; 1: 202-29.
55. Li W IT, Okada Y, Oku N, Kiwada H. Increased gene expression by cationic liposomes (TFL-3) in lung metastases following intravenous injection. *Biol Pharm Bull*. 2005; 28: 701-6.
56. Ross PC HS. Lipoplex size is a major determinant of in vitro lipofection efficiency. *Gene Ther*. 1999; 6: 651-9.
57. Ogris M SP, Kursa M, Mechtler K, Kircheis R, Wagner E. The size of DNA/transferrin-PEI complexes is an important factor for gene expression in cultured cells. *Gene Ther*. 1998; 5: 1425-33.
58. Schulze E, Ferrucci J, Poss K, LaPointe L, Bogdanova A, Weissleder R. Cellular uptake and trafficking of a prototypical magnetic iron oxide label in vitro. *Invest Radiol*. 1995; 30: 604-10.
59. Weissleder R, Cheng H-C, Bogdanova A, Bogdanov JA. Magnetically labeled cells can be detected by MR imaging. *J Magn Reson Imaging*. 1997; 7: 258-63.
60. Sun R, Dittrich J, Le-Huu M, Mueller M, Bedke J, Kartenbeck J, et al. Physical and biological characterization of superparamagnetic iron oxide- and ultrasmall superparamagnetic iron oxide-labeled cells: a comparison. *Invest Radiol*. 2005; 40: 504-13.
61. Weissleder R, Bogdanov A, Papisov M. Drug targeting in magnetic resonance imaging. *Magn Reson Q*. 1992; 8: 55-63.
62. Schaffer BK, Linker C, Papisov M, Tsai E, Nossiff N, Shibata T, et al. MION-ASF: biokinetics of an MR receptor agent. *Magn Reson Imaging*. 1993; 11: 411-7.
63. Shen TT, Bogdanov JA, Bogdanova A, Poss K, Brady TJ, Weissleder R. Magnetically labeled secretin retains receptor affinity to pancreas acinar cells. *Bioconjug Chem*. 1996; 7: 311-6.
64. Wilhelm C, Gazeau F, Bacri J. Magnetophoresis and ferromagnetic resonance of magnetically labeled cells. *Eur Biophys J*. 2002; 31: 118-25. doi:10.1007/s00249-001-0200-4.
65. Kuhlperter Rebecca M, Dahnke Hannes P, Matuszewski Lars M, Persigehl Thorsten M, von Wallbrunn Angelika P, Allkemper Thomas M, et al. R2 and R2\* Mapping for Sensing Cell-bound Superparamagnetic Nanoparticles: In Vitro and Murine in Vivo Testing. *Radiology*. 2007; 245: 449-57.
66. Tanimoto Akihiro M, Oshio Koichi M, Suematsu Makoto M, Poulliquen Daniel P, Stark David DM. Relaxation effect of clustered particles. *J Magn Reson Imaging* 2001; 14: 72-7.
67. Majumdar S, Zoghbi S, Pope C, Gore J. A quantitative study of relaxation rate enhancement produced by iron oxide particles in polyacrylamide gels and tissue. *Magn Reson Med*. 1989; 9: 185-202.
68. Perez JM, Simeone FJ, Saeki Y, Josephson L, Weissleder R. Viral-induced self-assembly of magnetic nanoparticles allows the detection of viral particles in biological media. *J Am Chem Soc*. 2003; 125: 10192-3.
69. Perez J, Josephson L, O'Loughlin T, Högemann D, Weissleder R. Magnetic relaxation switches capable of sensing molecular interactions. *Nat Biotechnol*. 2002; 20: 816-20. doi:10.1038/nbt720.
70. Simon G, Bauer J, Saborovski O, Fu Y, Corot C, Wendland M, et al. T1 and T2 relaxivity of intracellular and extracellular USPIO at 1.5T and 3T clinical MR scanning. *Eur Radiol*. 2006; 16: 738-45. doi:10.1007/s00330-005-0031-2.
71. Bowen C, Zhang X, Saab G, Gareau P, Rutt B. Application of the static dephasing regime theory to superparamagnetic iron-oxide loaded cells. *Magn Reson Med*. 2002; 48: 52-61. doi:10.1002/mrm.10192.
72. Shapiro M, Atanasijevic T, Faas H, Westmeyer G, Jasanoff A. Dynamic imaging with MRI contrast agents: quantitative considerations. *Magn Reson Imaging*. 2006; 24: 449-62. doi:10.1016/j.mri.2005.12.033.
73. Koenig S. Solvent relaxation by uniformly magnetized solute spheres. The classical-quantal connection. *Invest Radiol*. 1998; 33: 822-7.
74. Yablonskiy D, Haacke E. Theory of NMR Signal Behavior in Magnetically Inhomogeneous Tissues: The Static Dephasing Regime. *Magn Reson Med* 1994; 32: 749-63.

75. Verdijk P, Scheenen T, Lesterhuis W, Gambarota G, Veltien A, Walczak P, et al. Sensitivity of magnetic resonance imaging of dendritic cells for in vivo tracking of cellular cancer vaccines. *Int J Cancer*. 2007; 120: 978-84. doi:10.1002/ijc.22385.
76. Krieg FM, Andres RY, Winterhalter KH. Superparamagnetically labelled neutrophils as potential abscess-specific contrast agent for MRI. *Magnetic Resonance Imaging* 1995; 13: 393-400.
77. Walter G, Cahill K, Huard J, Feng H, Douglas T, Sweeney H, et al. Noninvasive monitoring of stem cell transfer for muscle disorders. *Magn Reson Med*. 2004; 51: 273-7. doi:10.1002/mrm.10684.
78. Boska M, Liu Y, Uberti M, Sajja B, Balkundi S, McMillan J, et al. Registered bioimaging of nanomaterials for diagnostic and therapeutic monitoring. *J Vis Exp*. 2010; 2459. doi:10.3791/2459.
79. Segers J, Laumonier C, Burtea C, Laurent S, Van der Elst L, Muller RN. From phage display to magnetophage, a new tool for magnetic resonance molecular imaging. *Bioconjug Chem* 2007; 18: 1251-8.
80. de Vries I, Lesterhuis W, Barentsz J, Verdijk P, van Krieken J, Boerman O, et al. Magnetic resonance tracking of dendritic cells in melanoma patients for monitoring of cellular therapy. *Nat Biotechnol*. 2005; 23: 1407-13. doi:10.1038/nbt1154.